A Steady State Thermodynamic Model of Concentrating Solar Power with Thermochemical Energy Storage

By

Brandon T. Gorman

A Thesis Presented in Partial Fulfillment
of the Requirements for the Degree
Master of Science

Approved April 2017 by the
Graduate Supervisory Committee

Nathan Johnson, Chair
Ellen Stechel
Mikhail Chester

ARIZONA STATE UNIVERSITY

May 2017

ABSTRACT

Fluids such as steam, oils, and molten salts are commonly used to store and transfer heat in a concentrating solar power (CSP) system. Metal oxide materials have received increasing attention for their reversible reduction-oxidation (redox) reaction that permits receiving, storing, and releasing energy through sensible and chemical potential. This study investigates the performance of a 111.7 MWe CSP system coupled with a thermochemical energy storage system (TCES) that uses a redox active metal oxide acting as the heat transfer fluid. A one-dimensional thermodynamic model is introduced for the novel CSP system design, with detailed designs of the underlying nine components developed from first principles and empirical data of the heat transfer media. The model is used to (a) size components, (b) examine intraday operational behaviors of the system against varying solar insolation, (c) calculate annual productivity and performance characteristics over a simulated year, and (d) evaluate factors that affect system performance using sensitivity analysis. Time series simulations use hourly direct normal irradiance (DNI) data for Barstow, California, USA. The nominal system design uses a solar multiple of 1.8 with a storage capacity of six hours for off-sun power generation. The mass of particles to achieve six hours of storage weighs 5,140 metric tonnes. Capacity factor increases by 3.55% for an increase in storage capacity to eight hours which requires an increase in storage volume by 33% or 737 m^3, or plant design can be improved by decreasing solar multiple to 1.6 to increase the ratio of annual capacity factor to solar multiple. The solar reduction receiver is the focal point for the concentrated solar energy for inducing an endothermic reaction in the particles under low partial pressure of oxygen, and the reoxidation reactor induces the opposite exothermic

reaction by mixing the particles with air to power an air Brayton engine. Stream flow data indicate the solar receiver experiences the largest thermal loss of any component, excluding the solar field. Design and sensitivity analysis of thermal insulation layers for the solar receiver show that additional RSLE-57 insulation material achieves the greatest increase in energetic efficiency of the five materials investigated.

ACKNOWLEDGMENTS

I am grateful for the dedication that my advisor, Prof. Nathan Johnson, has given to me by providing intellectual assistance, thoughtful understanding, and learning opportunities in the academic and scientific community. I look forward to continuing our endeavor to make the world a better place.

I am indebted to Prof. Tom Seager for believing in the potential of people, helping people make their ambitions become reality, and sharing this passion with me. I would certainly be less mindful if not for him.

I am thankful for Dr. Ellen Stechel for being such an intelligent scientist and for sharing her knowledge with me. However difficult it can be to keep pace with her mind, I always become more enlightened after our conversations.

The author would like to thank all the members of the PROMOTES team for useful conversations and insights, including Dr. James E. Miller, Prof. Hany Al Ansari, Dr. Andrea Ambrosini, Dr. Sean Babiniec, Dr. Eric Coker, Dr. Cliff Ho, Prof. Sheldon Jeter, Prof. Peter Loutzenheiser, and Andrew Shrader.

The U.S. Department of Energy (DOE) SunShot Initiative provided funding for the project entitled High Performance Reduction/Oxidation Metal Oxides for Thermochemical Energy Storage (PROMOTES) under award number DE-FOA-0000805-1541 as part of the CSP:ELEMENTS program.

Sandia is a multiprogram laboratory operated by Sandia Corporation, a Lockheed Martin Company, for the United States Department of Energy's National Nuclear Security Administration under contract DE-AC04-94AL85000.

TABLE OF CONTENTS

LIST OF TABLES

Table Page

LIST OF FIGURES

Figure Page

GENERAL NOMENCLATURE

Nomenclature	Units	Description
Δt	s	Time step length
i	-	Hourly time index
δ	-	Extent of reduction for particle
T_0	K	Ambient temperature
P_0	Pa	Ambient atmospheric pressure
P_{O_2}	Pa	Partial pressure of oxygen in ambient air
$P_{O_2}^{SR3}$	Pa	Partial pressure of oxygen inside SR3
N_p	mol	Total amount of particles in the system
$\dot{n}_p^{SR3}$	mol/s	Molar flow rate of particles through SR3
$\dot{n}_p^{ROx}$	mol/s	Molar flow rate of particles through ROx
$\dot{n}_{O_2}^{SR3}$	mol/s	Molar flow rate of oxygen leaving SR3
$\dot{m}_p^{SR3}$	kg/s	Mass flow rate of particles through SR3
M_p	kg/mol	Molar mass of particles
M_{air}	kg/mol	Molar mass of air
ρ_p	kg/m^3	Density of particles
$C_{P,p}$	J/mol-K	Specific heat of particles
ΔH_{rxn}	J/mol-O_2	Enthalpy of reduction per mole of oxygen created
R	J/mol-K	Universal gas constant
σ	W/m^2-K^4	Stefan-Boltzmann constant
g	m/s^2	Acceleration of gravity
H_{lift}	m	Total height of particle lift
η_{lift}	%	Electrical efficiency of particle lift
$Load_{lift}$	W	Parasitic load for lift operation
η_{pump}	%	Efficiency of vacuum pump
$Load_{pump}$	W	Parasitic load for vacuum pump operation
N^{pipe}	-	Number of pipes in the ROx
P_{comp}^{ROx}	Pa	Pressure of the ROx interior
$\dot{n}_{air}^{ROx}$	mol/s	Molar flow rate of air through ROx
L^{pipe}	m	Length of a ROx pipe
$D_{h,ins}^{ROx}$	m	Diameter for hot surface of ROx pipe insulation
t_{ins}^{ROx}	m	Thickness of ROx pipe insulation
k_{ins}^{ROx}	W/m-K	Thermal conductivity of ROx pipe insulation
D_p	m	Diameter of a particle
C_d	-	Drag coefficient
ϱ_p^{ROx}	%	Packing density of particles in a ROx pipe
$\vec{v}_{avg}^{ROx}$	m/s	Average velocity of particles and air
t_r^{ROx}	s	Total residence time of particles in a ROx pipe
t_{ox}^{ROx}	s	Residence time for chemical energy exchange in a ROx pipe
t_{ex}^{ROx}	s	Residence time for sensible energy exchange in a ROx pipe
DNI	W/m^2	Direct normal solar irradiance

DNI_{dp}	W/m^2	Direct normal solar irradiance used in design point system sizing
A_1^{sf}	m^2	Area of the solar field array at solar multiple of 1
A_{SM}^{sf}	m^2	Area of the solar field array at solar multiple of SM
SM	-	Ratio of the desired solar field area to the solar field area required to generate power at turbine rated capacity at design point DNI
η_{sf}	%	Collection efficiency of the solar field
ε_{ap}	-	Emissivity of the SR3 aperture
ε_{ins}	-	Emissivity of the SR3 insulation material
ε_{body}	-	Emissivity of the SR3 main body material
D_{win}	m	Diameter of each SR3 receiver window
F_{avg}	W/m^2	Average solar flux density at receiver aperture
L^{SR3}	m	Length of SR3 cavity
γ_{cav}	-	Ratio of the SR3 cavity surface area to aperture area
$r_{h,ins}^{SR3}$	m	Radius of hot surface of SR3 insulation
$r_{c,body}^{SR3}$	m	Radius of cold surface of SR3 main body
t_{ins}^{SR3}	m	Thickness of SR3 insulation
t_{body}^{SR3}	m	Thickness of SR3 main body
k_{ins}^{SR3}	W/m-K	Thermal conductivity of SR3 insulation
k_{body}^{SR3}	W/m-K	Thermal conductivity of SR3 main body
U^{HX}	W/m^2-K	Heat transfer coefficient of HX NTU method
A^{HX}	m^2	Contact surface area of HX
NTU^{HX}	-	Number of transfer units for HX
ϵ^{HX}	-	Effectiveness of HX
u	%	Extra volumetric ullage space for particle storage
ϱ_p	%	Packing density of particles in storage
V^{HS}	m^3	Total volume of HS bin
HD^{HS}	-	Ratio of height to diameter for HS bin
t_{ins}^{HS}	m	Thickness of HS insulation
k_{ins}^{HS}	W/m-K	Thermal conductivity of HS insulation
V^{CS}	m^3	Total volume of CS bin
HD^{CS}	-	Ratio of height to diameter for CS bin
t_{ins}^{CS}	m	Thickness of CS insulation
k_{ins}^{CS}	W/m-K	Thermal conductivity of CS insulation
CF_{sys}	%	System-wide capacity factor
$\eta_{E,ROx}$	%	ROx component energy efficiency
$\eta_{E,cc}$	%	Power block combined cycle energy efficiency

1. INTRODUCTION

The three renewable power sectors with largest installed capacities in the world are hydropower, wind power, and solar power [1]. Of these three types, hydropower has the most generation capacity and solar power has the least generation capacity [1]. This ranking is expected to reverse in the United States because the wind power sector is expected to exceed the hydropower sector by 2040 and the solar power sector is expected to grow by 221 GW through 2040 to exceed wind power and hydropower sectors [2]. This growth of solar in the United States is in large part due to the continued price reductions of soft and hardware costs for residential, commercial, and utility solar photovoltaics (PV) markets [3]. Comparatively, worldwide solar PV installed capacity is expected to more than triple from 228 GW in 2015 to 756 GW by 2025 [4, 5]. Large-scale concentrating solar power (CSP) systems continue to be attractive options for utility-scale generation in locations with abundant direct solar radiation because they can integrate thermal energy storage, and provide peak, flexible, and base-load power [6, 7].

Solar CSP field designs include power towers, parabolic troughs, linear fresnel, and parabolic dishes. Power towers have the greatest potential for future development because they can operate at higher temperatures, and thereby higher efficiencies, than the commercially proven parabolic trough systems [8]. Power tower systems include four major components: (1) a solar field for concentrating solar energy onto a solar receiver located on the tower, (2) the tower and receiver, (3) heat transfer fluid (HTF) and storage media, and (4) a power block for converting thermal energy into electrical power. The optional storage component can be used to increase plant productivity, mitigate intermittency in the solar resource, and extend power production to off-sun hours to

increase plant capacity factor, at roughly the same levelized cost of energy as without storage [9, 10]. These thermal storage schemes—e.g. storing of sensible energy in a heated fluid—are useful for generating electric power during off-sun hours, i.e. after sunset and before sunrise, or transient clouding effects because they can be recharged on a daily basis and discharged during periods of low solar irradiance.

CSP systems with storage allow utilities to plan and schedule solar power plants similar to traditional dispatchable fossil-fueled generation units [11, 12]. As utilities seek options to avoid "duck curve" events in the system net load profile that occurs when solar power output declines in the late afternoon and residential loads increase as people arrive home from work or school, storage can be used to shift solar generation from the usual hours of high solar output to those of low solar output [13]. While power tower systems can achieve 35% capacity factor without storage, up to 80% capacity factor can be achieved for plants with storage due to extended hours of operation [14]. However, the delivered energy cost of CSP between 12.5 and 16.4 cents per kWh is higher than solar photovoltaic (PV) at 11.0 cents per kWh [14]. Ongoing research in advanced HTFs is seeking to provide a significant drop in the cost of energy from CSP systems. Fundamental research in new HTFs is permitting the development of novel CSP system design configurations with new design alternatives for heat transfer loops, thermal energy storage, and power blocks.

This study investigates the performance of a 111.7 MWe CSP system coupled with a thermochemical energy storage system (TCES) that uses a redox active metal oxide acting as the HTF. A one-dimensional thermodynamic model is introduced for the novel CSP system design, with detailed designs of the underlying nine components

developed from first principles and empirical data of the heat transfer media. The model is used to (a) size components, (b) examine intraday operational behaviors of the system against varying solar insolation, (c) calculate average productivity and performance characteristics over a simulated year, and (d) evaluate factors that affect system performance using sensitivity analysis. Results demonstrate applications of this technology for electrical power generation and discuss the potential for future commercialization. Efforts in this work also advance science to draw closer to U.S. Department of Energy (DOE) SunShot Initiative targets for a levelized cost of energy (LCOE) under 6 cents per kWh, without subsidies, by the year 2020 [15]. Work presented in this study is developed from U.S. DOE funding for the High Performance Reduction Oxidation of Metal Oxides for Thermochemical Energy Storage (PROMOTES) project of the ELEMENTS portfolio [16].

2. BACKGROUND

Concentrating solar power (CSP) systems commonly use heat transfer fluids (HTFs) such as steam, oil, molten salt, or air to transfer solar energy to the power block of a CSP power plant. The fluids typically capture solar thermal energy as sensible energy using the heat capacity of the fluid. High temperature fluids are ideal for power cycle efficiency and plant economics. Limitations to HTF temperatures include plant design (e.g., solar receiver geometry and materials) and fluid characteristics (e.g., mode of heat transfer, fluid attrition, decomposition). There can be several fluids used in a single CSP system—e.g., HTF in the solar field (oil), thermal energy storage material (molten salt), and working fluid in the power block (steam) [17].

Molten nitrate salt is an effective HTF due to thermal stability, low vapor pressure and viscosity, and high thermal conductivity as a liquid in the temperature range of 220 °C to 565 °C [17, 18, 19]. Molten salts are most common in power tower CSP systems, and synthetic oils are most common in parabolic trough and linear Fresnel concentrator CSP systems [20]. Molten salts, when compared to synthetic oils, have better energy storage capacities due to superior heat transfer capabilities and higher temperatures of operation. Sensible energy absorption, however, is limited by the maximum HTF temperature which, in turn, limits molten salt and thermal oil energy density. Energy density can be increased by using phase changing fluids that undergo a state change—e.g., solid to liquid or liquid to gas—using the latent heat of fusion and vaporization [21, 22].

Phase changing fluids can include materials that undergo solid-solid, solid-liquid, and liquid-gas transition [23]. Materials that undergo solid-liquid transitions, however,

are more practical due to their lower volumetric expansion compared to liquid-gas [23]. Solid phase materials generally have low thermal conductivity, however, posing a challenge during the heat transfer process—the poor power capacity of such materials might offset the benefit of higher energy density. This makes phase changing materials an unlikely alternative to oil and molten salt in power tower and linear concentrator systems where heat transfer to the engine generally does not occur at constant temperature. Dish-Stirling engine systems may use phase changing materials for the HTF, since heat transfer to the engine occurs at constant temperature [24, 25].

Materials that undergo reversible chemical reactions—reactants absorb heat to undergo an endothermic reaction and in the reverse exothermic reaction releases heat by returning to the initial state—are also attractive options to increase energy density [26]. Chemically reactive materials that undergo reversible thermochemical reactions can be used to capture solar thermal energy as a combination of sensible energy and an endothermic chemical reaction, stored as high energy density products in an optional step, and release the captured energy into the power block during the reverse exothermic chemical reaction. Such materials must withstand material attrition for a large number of reversible thermochemical cycles. Cutting edge solar energy research is evaluating the scientific applications and commercialization of these reversible thermochemical reactions using reduced metal oxide particles [27, 28, 29]. This paper here investigates redox-active metal oxides that are mixed ionic-electronic conductors (MIEC). The MIEC redox active metal oxides have several advantages that make them attractive options for use as HTFs, which include:

- Swift utilization of bulk particles—Fast oxygen ion transport facilitates rapid and complete utilization—the redox reactions of the metal oxides are not surface limited.
- Capability to reach higher temperatures—Metal oxides maintain stability at temperatures higher than oil and molten salt, and thereby can increase system efficiency (e.g., Carnot cycle efficiency).
- High energy density in storage—Materials that store a combination of sensible and chemical energy have the potential to exceed energy stored in sensible only or phase changing materials.
- Stability over a large number of cycles—MIEC conductors allow manipulation of thermophysical parameters that influence their redox kinetics and operating temperatures, while resisting redox attrition over life cycle of plant operation.
- Use of combined cycle in the power block—Redox active metal oxides can release heat through an exothermic re-oxidation reaction by interacting with oxygen (air) in an open gas turbine system with a bottoming Rankine cycle for added efficiency. Hybridization of the combined cycle is possible, i.e. firing of natural gas to continue power production after storage has been fully discharged.

These 5 properties permit the modeling, design, and evaluation of a novel CSP system that uses reversible thermochemical reactions and new types of component configurations.

2.1. Reversible Thermochemical Reactions

Stoichiometry of the metal oxide redox reaction is simple, and produces (requires) only oxygen gas as a bi-product (reactant). The metal oxides typically operate as solid

thermochemical reactants and products for temperatures up to 1000 °C [27]. Plant design can be simplified for solid HTFs that only require radiation-solid and solid-gas interfaces compared with the liquid pumping mechanisms required for oil and molten salt [30]. Equation 1.0 below shows the general equation for the metal oxide (in this case a perovskite MIEC) reduction/oxidation reaction where the reduction extent (δ) increases as equilibrium shifts to the right [31, 32]:

$$\frac{1}{\delta} ABO_{3-x} \leftrightarrow \frac{1}{\delta} ABO_{3-x-\delta} + \frac{1}{2} O_2(g) \tag{1.0}$$

Reduction extent, δ, for the above reaction ranges on a continuous scale 0 and above. At 0 the metal oxides remain fully oxidized and no oxygen is produced, and at 3 the entirety of the reactant is reduced to produce the maximum amount of oxygen gas possible (2:1 ratio of metal oxide formula units to oxygen molecules). In practice, the oxides should not deviate substantially from their oxidized crystal structure, and the metal oxides do not approach a fully reduced state to the metals (formal valence of 0). Hence, there is a maximum δ for which the material retains the perovskite structure while creating vacancies on the anion lattice, and the reducible metals do not reduce beyond +2 formal valence.

2.2. Innovation in CSP System Design

Systems modeling can be viewed as a hierarchy: at the bottom are detailed input parameters that feed into component and process models in the middle, which, in turn, feed into total system models at the top that evaluate metrics such as levelized cost of energy (LCOE) and/or power output [33]. Twenty-one CSP modeling packages were

identified, some of which specialize on a single task, like Dish Field Systems Model, and some of which use component performance models to measure systems technoeconomics, like System Advisor Model (SAM) [33, 34].

China is developing models of central receiver systems using a new solar collection field model called HFLD coupled with a plant modeled (heliostat, tower receiver, and power cycle) based on energy balances using TRNSYS [35, 36] The cavity receiver considers losses due to radiation and convection, but not conduction. The overall heat transfer coefficient used, however, is an empirically fitted equation. The plant operation consists of 7 states: shut down, standby, start-up, normal operation, charging storage, discharging storage, and load rejection.

A 50 MWe parabolic trough model (solar field, heat transfer piping, power block, and energy storage) was simulated using Mathematica 7 and compared to an equivalent plant in Spain [37]. Receiver losses and piping losses are modeled using an empirically fitted equation. The power block heat exchanger uses a flat efficiency term, and the turbine efficiency uses an equation fitted to manufacturer provided data. Parasitic loads such as pumps and lifts were not considered.

A technoeconomic systems model of a 200 MWe power tower with phase change materials (PCM) using highly detailed component performance models was simulated in FORTAN and compared to SAM generated results [38, 39, 40]. The model considered two types of latent thermal energy storage for the PCM coupled with steam and supercritical CO_2 of power cycles. The optimal dimensions of the storage units, using thermal circuits for the materials, were investigated with respect to plant capacity factor, exergetic efficiency, and LCOE.

The work presented here, written in Python, uses the bottom-up methodology of highly detailed thermodynamic equations including thermal circuits coupled with component energy balances to investigate annual system energy efficiency and capacity factor performance metrics. A 100 MWe power tower with new thermochemical heat absorption material and energy storage is simulated. System energy efficiency investigated here includes the solar collection field efficiency, thermal efficiency of the central receiver subsystem, auxiliary loads efficiency using the parasitic vacuum pump and particle lift work for plant operation, and combined cycle power block efficiency. The solar collection field efficiency is assumed as an average value, and the power block input/output states, and thus efficiency, are taken from manufacturer provided specifications.

Future work can expand the system design parameter inputs to investigate performance metrics in higher levels of detail, and technoeconomics by coupling materials and designs with cost equations. Economics, like balance of plant costs, can limit overall systems design due to economic constraints, and material properties such as material attrition, corrosion, and thermochemical stress that inhibit fluid energy density can limit overall systems designs due to energy efficiency constraints [41].

3. METHODOLOGY

A one-dimensional energy and mass balance around nine components of the CSP system results in an equation set for systems-level evaluation using design point and time series simulations of system operation and performance. The thermodynamics of each component of the CSP is written and developed in Python. Fluid properties are sampled at component specific operating temperatures and pressures using the CoolProp module [42]. An external Engineering Equation Solver (EES) model was used to balance the thermodynamic operation of the power block subsystem, and feed the output state information into the main CSP systems model.

3.1. Systems Model Development

Figure 1 shows the component diagram of the PROMOTES system that depicts the process of converting solar thermal energy shining on the solar collection field, concentrated into an endothermic solar receiver, hot particles transported to an exothermic reactor, and hot, pressurized air fed into a turbine to generate electric power [16]. Figure 2 details a block component diagram with input and output stream flows, and shows the subsystem boundary modeled in detail here. This subsystem boundary includes the reoxidation reactor, reduction receiver reactor, hot storage, cold storage, heat exchanger, vacuum pump, and particle lift, as well as their interconnecting mass and energy streams. A solar collection field and air Brayton turbine with a bottoming steam cycle are two additional subsystems outside of this boundary. These two components lie outside the subsystem boundary, and, thus, use simplified state and energy equations.

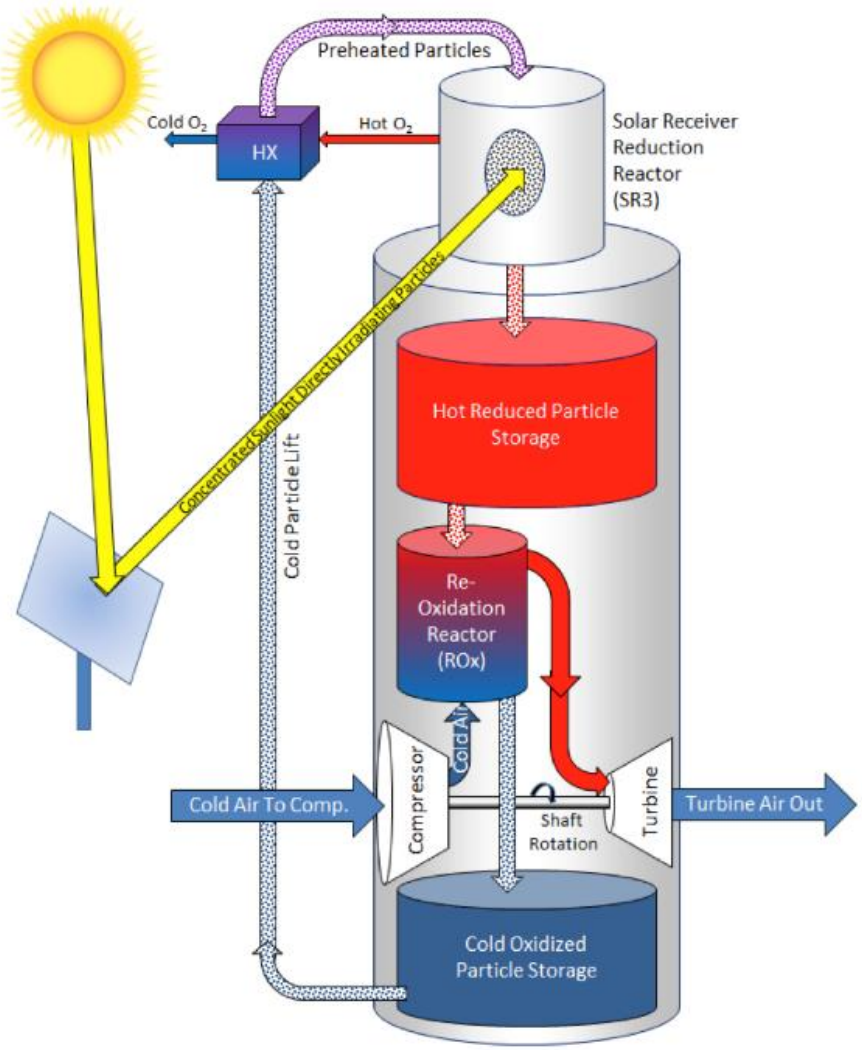

Figure 1. Component diagram of the PROMOTES system

The quasi-steady state thermodynamic is comprised of 28 states. Each component has input and output states; some states may lie outside the subsystem boundary, however. The energy and mass balance about each component is solved independently or may require an iterative solution—e.g., the oxygen and particle streams between the SR3 and HX components are interdependent. The mass (thermal) energy streams directions are depicted using a blue arrow, the thermal energy streams are depicted using a yellow arrow, and the work energy stream are depicted using an orange arrow.

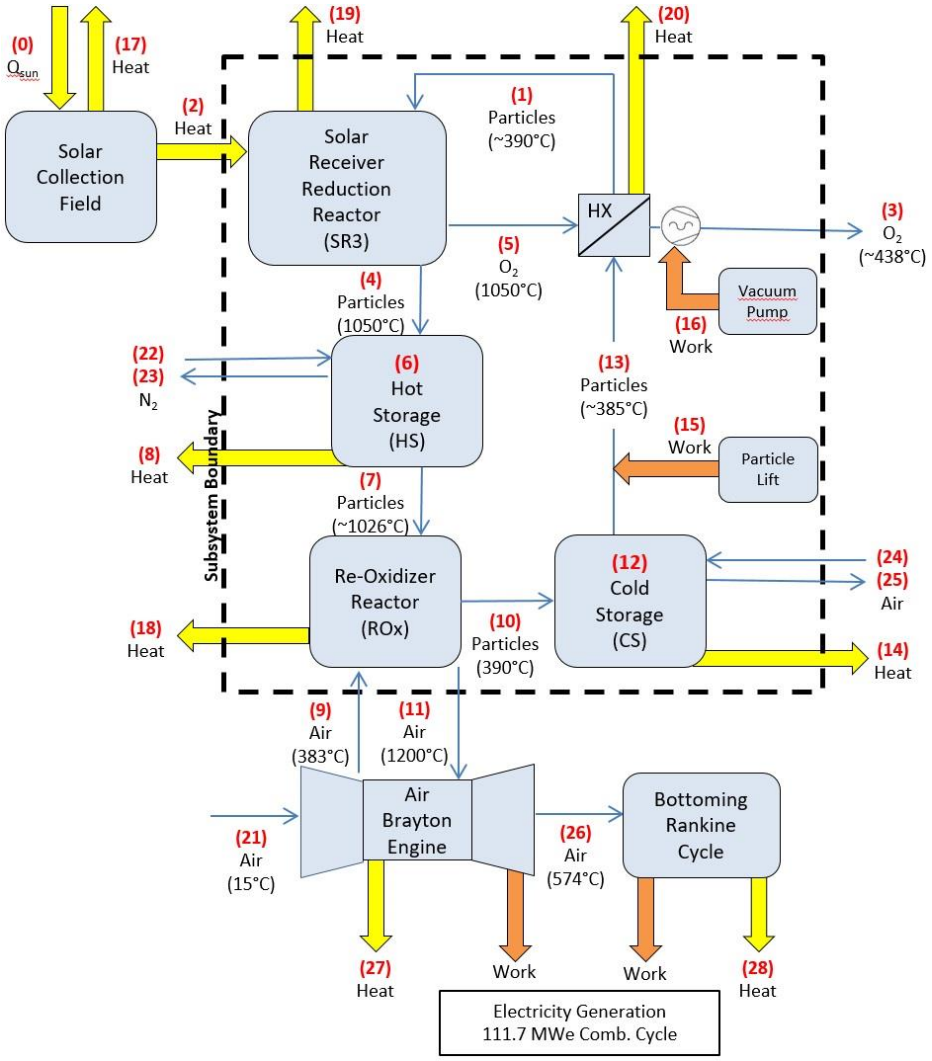

Figure 2. Schematic of components and streams included in the PROMOTES systems model

Re-Oxidation Reactor (ROx): Reacts hot reduced metal oxide particles with pressurized oxygen (air) in counter-flow to induce an exothermic reaction and exchange heat in a reaction chamber. The resulting exiting high temperature air enters the air Brayton engine for power generation. Five energy streams for the ROx are balanced in Eq. 2.0. Energy streams include the inlet particle flow ($\dot{E}_7$), inlet air flow ($\dot{E}_9$), outlet particle flow ($\dot{E}_{10}$), outlet air flow ($\dot{E}_{11}$), and heat loss ($\dot{E}_{18}$). The heat loss term for stream 18 is modeled using three thermal resistances in series: convection to insulation,

conduction through insulation, and then convection to ambient air. Note that total convective losses depend on the number of ROx pipes (N^{pipe}), because more pipes for the same cross-sectional areas has greater surface area by a factor of $\sqrt{N^{pipe}}$. The current equation set assumes that both the pressure drop and air mass decrease across the ROx is negligible, therefore temperature and pressure states are held constant for the properties of air.

$$\Delta\dot{E}_{ROx} = 0 = \dot{E}_7 + \dot{E}_9 - \dot{E}_{10} - \dot{E}_{11} - \dot{E}_{18} \tag{2.0}$$

Solar Receiver Reduction Reactor (SR3): Captures the concentrated solar radiation at multiple towers to heat and reduce (to a reduction extent of δ) the metal oxide particles (ABO_{3-x} to $ABO_{3-x-\delta}$) in an endothermic reaction given in Eq. 1.0 and balanced in Eq. 2.1. Five energy streams for the SR3 are balanced in Eq. 2.1. Energy streams include the inlet particle flow ($\dot{E}_1$), the incoming concentrated solar flux ($\dot{E}_2$), the outlet particle flow ($\dot{E}_4$), the outlet oxygen flow ($\dot{E}_5$), and heat loss ($\dot{E}_{19}$). The heat loss equation for stream 19 is due to re-radiation losses through the aperture window and thermal losses modeled with three thermal resistances in series with additional radiative layer: conduction through insulation, radiative heat transfer through evacuated space, conduction through main body, and convection to ambient air. Note that total convective losses depend on the total surface area of all the cavity receivers which, in turn, depends on the size of the solar collection field area (A_{SM}^{sf}) and average solar flux density (F_{avg}).

$$\Delta\dot{E}_{SR3} = 0 = \dot{E}_1 + \dot{E}_2 - \dot{E}_4 - \dot{E}_5 - \dot{E}_{19} \tag{2.1}$$

Heat Exchanger (HX): Recuperates heat from high temperature oxygen exiting the SR3 to preheat metal oxide particles discharging from cold storage. Five energy

streams for the HX are balanced in Eq. 2.2. Energy streams include the outlet particle flow ($\dot{E}_1$), the outlet oxygen flow ($\dot{E}_3$), the inlet oxygen flow ($\dot{E}_5$), the inlet particle flow ($\dot{E}_{13}$), and heat loss ($\dot{E}_{20}$). The heat exchanger equation uses the number of transfer units (NTU) method to calculate the effectiveness of a counter-current flow heat exchanger.

$$\Delta\dot{E}_{HX} = 0 = \dot{E}_5 + \dot{E}_{13} - \dot{E}_1 - \dot{E}_3 - \dot{E}_{20} \tag{2.2}$$

Hot Storage (HS): Stores hot, reduced metal oxide particles. Storage is charged (filled) during on-sun hours and discharged (emptied) during off-sun hours—e.g., after sunset. One storage term and five energy streams for the HS are balanced in Eq. 2.3. The storage term is for the hot, reduced particles with an inert nitrogen gas blanket (E_6 and $\dot{E}_6$). Energy streams include the inlet particle flow ($\dot{E}_4$), the outlet particle flow ($\dot{E}_7$), heat loss ($\dot{E}_8$), the inlet nitrogen flow ($\dot{E}_{22}$), and the outlet nitrogen flow ($\dot{E}_{23}$). The heat loss equation for stream 8 is modeled as three thermal resistances of the cylindrical hot bin in parallel: resistance through the upper surface, radial resistance through the side, and resistance through the lower surface. For the purposes of the model, each of these resistance terms consist of two thermal resistances in series: conduction through insulation and convection to ambient air.

$$E_{HS}^{i} = E_6^{i-1} + \Delta t \cdot \left(\dot{E}_6^{i-1} + \dot{E}_4^{i-1} - \dot{E}_7^{i-1} - \dot{E}_8^{i-1} + \dot{E}_{22}^{i-1} - \dot{E}_{23}^{i-1}\right) \tag{2.3}$$

Cold Storage (CS): Stores cold, oxidized metal oxide particles. Storage is charged (filled) and discharged (emptied) as hot storage is emptied and filled, respectively. One storage term and five energy streams for the CS in are balanced in Eq. 2.4. The storage term is for the cold, oxidized particles mixed with air (E_{12} and $\dot{E}_{12}$). Energy streams include the inlet particle flow ($\dot{E}_{10}$), the outlet particle flow ($\dot{E}_{13}$), heat loss ($\dot{E}_{14}$), the

inlet air flow ($\dot{E}_{24}$), and the outlet air flow ($\dot{E}_{25}$). The heat loss equation for stream 14 is due to three thermal resistances of the cylindrical cold bin in parallel: resistance through the upper surface, radial resistance through the side, and resistance through the lower surface. Again, for the purposes of the model, each of these resistance terms consist of two thermal resistances in series: conduction through insulation and convection to ambient air.

$$E_{CS}^{i} = E_{12}^{i-1} + \Delta t \cdot \left(\dot{E}_{12}^{i-1} + \dot{E}_{10}^{i-1} - \dot{E}_{13}^{i-1} - \dot{E}_{14}^{i-1} + \dot{E}_{24}^{i-1} - \dot{E}_{25}^{i-1}\right) \tag{2.4}$$

Particle Lift: Carries cold, oxidized particles upward to enter at the top of the SR3. The work terms are considered auxiliary power loads with parasitic losses and are not used in energy balance equations around the components, however, they affect net system productivity and total system efficiency. The work stream for the particle lift ($\dot{E}_{15}$) is converted to energy in Eq. 2.5 using the molar flow rate to mass flow rate conversion in Eq. 2.6 and a constant parasitic load term.

$$\dot{E}_{15} = \dot{m}_p^{SR3} \cdot g \cdot H_{lift} \cdot \frac{1}{\eta_{lift}} + Load_{lift} \tag{2.5}$$

$$\dot{m}_p^{SR3} = \dot{n}_p^{SR3} \cdot M_p \tag{2.6}$$

Vacuum Pump: Evacuates oxygen produced in the SR3, thereby maintaining a low partial pressure of oxygen to induce the reduction reaction. The work stream demand for the vacuum pump ($\dot{E}_{16}$) is converted to electrical energy in Eq. 2.7 and a constant parasitic load term.

$$\dot{E}_{16} = \dot{n}_{O_2}^{SR3} \cdot R \cdot T_0 \cdot \ln\left(\frac{P_0}{P_{O_2}^{SR3}}\right) \cdot \frac{1}{\eta_{pump}} + Load_{pump} \tag{2.7}$$

Solar Field: Collects incident sunlight and concentrates the reflected radiation into the SR3. The concentrated solar energy entering the SR3 ($\dot{E}_2$) depends on the magnitude of solar irradiance ($\dot{Q}_{sun}$), size of solar field area, and the collection efficiency term in Eq. 2.8.

$$\dot{Q}_{sun} - \dot{E}_{17} = \dot{E}_2 = DNI \cdot A_{SM}^{sf} \cdot \eta_{sf} \tag{2.8}$$

Power Block: Generates electricity using a heat transfer fluid, in this case the pressurized heated air exiting the ROx. Manufacturer specified ratings such as gross rated power output for single-cycle and combined-cycle generation, air mass flow rate, turbine outlet temperature, and compression ratio are used to validate and calculate compressor air outlet temperature and turbine inlet temperature using an externally developed model explained in section 3.1.7.

3.1.1. Initial Systems Equations

The molar flow rate of metal oxide particles is abbreviated across streams 1, 4, and 13 as $\dot{n}_p^{SR3}$ and across streams 7 and 10 as $\dot{n}_p^{ROx}$ shown in Fig. 2, because they are equivalent for the states in this simplified nomenclature. The temperature states are denoted as T with ambient temperature denoted as T_0. The stored chemical energy of the redox reaction is the enthalpy of reduction per mole of oxygen gas and is denoted as H_{rxn}. Sensible energy is tracked across temperature changes using the specific heat capacity of the metal oxide particles (approximated as a constant independent of temperature and independent of δ), oxygen, and air denoted as $C_{P,p}$, C_{P,O_2}, and $C_{P,air}$, respectively. Table 1 below provides a list and definition for system-wide variables and

attributes used throughout the system's model equations. Tables 2 to 6 are variables and attributes that are specific to system components.

Table 1. Nomenclature of system wide variables and attributes

Nomenclature	Units	Description
Δt	s	Time step length
$\dot{E}_0$	W	Solar flux into solar collection field
$\dot{E}_1$	W	Energy stream for particles from HX to SR3
$\dot{E}_2$	W	Solar flux into SR3
$\dot{E}_3$	W	Energy stream for oxygen exhausted from HX
$\dot{E}_4$	W	Energy stream for particles from SR3 to HS
$\dot{E}_5$	W	Energy stream for oxygen from SR3 to HX
E_6^t	J	Energy stored in the HS bin at time step t
$\dot{E}_7$	W	Energy stream for particles from HS to ROx
$\dot{Q}_8$	W	Convective heat loss from HS
$\dot{E}_9$	W	Energy stream for air from Brayton engine to ROx
$\dot{E}_{10}$	W	Energy stream for particles from ROx to CS
$\dot{E}_{11}$	W	Energy stream for air from ROx to Brayton engine
E_{12}^t	J	Energy stored in the CS bin at time step t
$\dot{E}_{13}$	W	Energy stream for particles from CS to HX
$\dot{Q}_{14}$	W	Convective heat loss from CS
$\dot{E}_{15}$	W	Energy stream to operate lift moving particles from CS to HX
$\dot{E}_{16}$	W	Energy stream to operate vacuum pump
$\dot{E}_{17}$	W	Heat loss from the solar collection field
$\dot{E}_{18}$	W	Convective heat loss from ROx
$\dot{E}_{19}$	W	Radiative and convective heat loss from SR3
$\dot{E}_{20}$	W	Heat loss from HX
$\dot{E}_{21}$	W	Energy stream for ambient air into Brayton engine
$\dot{E}_{22}$	W	Energy stream for nitrogen into HS
$\dot{E}_{23}$	W	Energy stream for nitrogen exhausted from HS
$\dot{E}_{24}$	W	Energy stream for air into CS
$\dot{E}_{25}$	W	Energy stream for air exhausted from CS
$\dot{E}_{26}$	W	Energy stream for air exhausted from Brayton engine
$\dot{E}_{27}$	W	Heat loss from the air Brayton engine
$\dot{E}_{28}$	W	Heat loss from the bottoming Rankine cycle
T_0	K	Ambient atmospheric temperature
T_1	K	Temperature of particles from HX to SR3
T_3	K	Temperature of oxygen exhausted from HX
T_4	K	Temperature of particles from SR3 to HS
T_5	K	Temperature of oxygen from SR3 to HX
T_6	K	Temperature of particles and nitrogen in HS

T_7	K	Temperature of particles from HS to ROx
T_9	K	Temperature of air from Brayton engine to ROx
T_{10}	K	Temperature of particles from ROx to CS
T_{11}	K	Temperature of air from ROx to Brayton engine
T_{12}	K	Temperature of particles and air in CS
T_{13}	K	Temperature of particles from CS to HX
T_{20}	K	Temperature of air from Brayton engine to Rankine cycle
T_{21}	K	Temperature of ambient air into Brayton engine
P_0	Pa	Ambient atmospheric pressure
P_{O_2}	Pa	Partial pressure of oxygen in ambient air
$P_{O_2}^{SR3}$	Pa	Partial pressure of oxygen inside SR3
N_p	mol	Total amount of particles in the system
$\dot{n}_p^{SR3}$	mol/s	Molar flow rate of particles through SR3
$\dot{n}_p^{ROx}$	mol/s	Molar flow rate of particles through ROx
$\dot{n}_{O_2}^{SR3}$	mol/s	Molar flow rate of oxygen leaving SR3
M_p	kg/mol	Molar mass of particles
M_{air}	kg/mol	Molar mass of air
$\dot{m}_p^{SR3}$	kg/s	Mass flow rate of particles in the elevator
ρ_p	kg/m^3	Density of particles
$C_{P,p}$	J/mol-K	Specific heat of particles
C_{P,O_2}	J/mol-K	Specific heat of oxygen
$C_{P,air}$	J/mol-K	Specific heat of air
δ	-	Reduction extent of particles
ΔH_{rxn}	J/mol-O_2	Enthalpy of reduction per mole of oxygen created
u	%	Extra volumetric ullage space for particle storage
ϱ_p	%	Packing density of particles in storage
H_{lift}	m	Total height of particle lift
η_{lift}	%	Electrical efficiency of particle lift
η_{pump}	%	Electrical efficiency of vacuum pump
R	J/mol-K	Universal gas constant
σ	W/m^2-K^4	Stefan-Boltzmann constant
g	m/s^2	Acceleration of gravity
k_{air}	W/m-K	Thermal conductivity of air
ν_{air}	m^2/s	Kinematic viscosity of air
α_{air}	m^2/s	Thermal diffusivity of air
Pr_{air}	-	Prandtl number of air

The extent of reduction is calculated in Eq. 3.0 below using an empirical relation. Equation 3.1 provides an intermediate variable related to the vacuum pump and is calculated from the partial pressure of oxygen in ambient air and the partial pressure of

oxygen in the SR3. Equation 3.2 uses a reference temperature of 673.15 °K and the high reduction temperature of the SR3 system.

$$\delta = e^{-\left(\frac{7.49697-10.7886\cdot\partial_B+6.68975\cdot\left(e^{\partial_B}-1.0-\partial_B\right)-0.292324\cdot\partial_A+0.319622\cdot\partial_A\cdot\partial_B}{1.0+0.104546\cdot\partial_A}\right)} - 0.000574 \tag{3.0}$$

$$\partial_A = 0.5 * ln\left(\frac{P_{O_2}}{P_{O_2}^{SR3}}\right) \tag{3.1}$$

$$\partial_B = -ln\left(\frac{673.15}{T_4}\right) \tag{3.2}$$

The user inputs the solar multiple of the simulation to increase or decrease the size of the solar field. At a solar multiple of 1, the solar field is sized to generate rated power at the design point DNI (A_1^{sf}). Thus, the solar field sized at a solar multiple of 1 is used as a reference point. The equation for converting solar field sized at a solar multiple of 1 and the solar multiple into the solar field size used in the simulation is expressed in Eq. 3.3.

$$A_{SM}^{sf} = SM \cdot A_1^{sf} \tag{3.3}$$

The ROx, SR3, HS, and CS components use thermal resistance terms to determine the amount of heat loss. Thermal circuits may be a composite of series and parallel resistances that can be aggregated to a total thermal resistance term. The heat transfer rate is an intermediate term used to calculate heat loss from total thermal resistance. The heat transfer rate equation expressed in Eq. 3.4 uses the overall heat transfer coefficient, contact area, and overall temperature difference terms. The total thermal resistance equation expressed in Eq. 3.5 is simply the multiplicative inverse of the overall heat transfer coefficient and the contact area.

$$\dot{Q} = U \cdot A \cdot \Delta T \tag{3.4}$$

$$R_{tot} = \frac{1}{U \cdot A} \tag{3.5}$$

3.1.2. Equations for the Re-Oxidizer Reactor (ROx)

The five energy streams entering and exiting the ROx balanced in Eq. 4.0, include the inlet particle flow (stream 7), the inlet air flow (stream 9), the outlet particle flow (stream 10), the outlet air flow (stream 11), and heat loss (stream 18). Particles are in direct contact with air flowing counter-current in each pipe within the ROx. Numerous pipes comprise the full reactor. A heat loss term is modeled using three thermal resistances in series: internal convection to insulation, conduction through insulation, and then convection to external ambient air. Convective losses from a single pipe are calculated and then summed to compute total convective losses from the ROx. The equation set assumes that pressure drop and mass flow loss across the ROx are negligible. Air properties are evaluated at the ROx mean temperature and internal pressure of the ROx compressor. Constant specific heat is assumed. All streams energy flow rates in Eqs. 4.1 to 4.6 are expressed with reference to ambient conditions.

Table 2. Nomenclature for ROx component variables and attributes

Nomenclature	Units	Description
$\dot{E}_{ROx}$	W	Energy balance about ROx
N^{pipe}	-	Number of pipes in the ROx
$T_{c,ins}^{ROx}$	K	Cold-surface temperature of ROx insulation
$T_{h,ins}^{ROx}$	K	Hot-surface temperature of ROx insulation
$T_{f,c,ins}^{ROx}$	K	Film temperature of ROx insulation with ambient air
$T_{f,h,ins}^{ROx}$	K	Film temperature of ROx insulation with hot, turbulent air
T_{avg}^{ROx}	K	Mean temperature of ROx
P_{comp}^{ROx}	Pa	Pressure of the ROx interior
$\dot{n}_{air}^{ROx}$	mol/s	Molar flow rate of air through ROx
R_{tot}^{ROx}	W/K	Total thermal resistance of ROx

$R_{h,conv}^{ROx}$	W/K	Thermal resistance of ROx hot, turbulent air convection
R_{ins}^{ROx}	W/K	Thermal resistance of ROx insulation conduction
$R_{c,conv}^{ROx}$	W/K	Thermal resistance of ROx ambient air convection
L^{pipe}	m	Length of a ROx pipe
$D_{h,ins}^{ROx}$	m	Diameter for hot surface of ROx pipe insulation
$r_{c,ins}^{ROx}$	m	Radius to cold surface of ROx pipe insulation
$r_{h,ins}^{ROx}$	m	Radius to hot surface of ROx pipe insulation
t_{ins}^{ROx}	m	Thickness of ROx pipe insulation
$A_{c,ins}^{ROx}$	m^2	Area for cold, convective surface of ROx pipe insulation
$A_{h,ins}^{ROx}$	m^2	Area for hot, convective surface of ROx pipe insulation
k_{ins}^{ROx}	W/m-K	Thermal conductivity of ROx pipe insulation
μ_{air}	Pa−s	Viscosity of air
$Ra_{c,ins}^{ROx}$	-	Rayleigh number of ROx pipe contact surface with ambient air
$Re_{h,ins}^{ROx}$	-	Reynolds number of ROx pipe contact surface with hot, turbulent air
$Nu_{c,ins}^{ROx}$	-	Nusselt number of ROx pipe contact surface with ambient air
$Nu_{h,ins}^{ROx}$	-	Nusselt number of ROx pipe contact surface with hot, turbulent air
$h_{c,ins}^{ROx}$	W/m^2-K	Heat transfer coefficient of ROx pipe insulation with ambient air
$h_{h,ins}^{ROx}$	W/$m^2$0K	Heat transfer coefficient of ROx pipe insulation with hot, turbulent air
D_p	m	Diameter of a particle
A_p	m^2	Projected area of a particle
V_p	m^3	Volume of a single particle
ρ_{air}	kg/m^3	Density of air
m_p	kg	Mass of a single particle
C_d	-	Drag coefficient
$\dot{m}_p^{pipe}$	kg/s	Mass flow rate of particles through a ROx pipe
$\dot{m}_{air}^{pipe}$	kg/s	Mass flow rate of air through a ROx pipe
ϱ_p^{ROx}	%	Packing density of particles in a ROx pipe
$\vec{v}_{term}^{ROx}$	m/s	Terminal velocity of particles relative to air
$\vec{v}_p^{ROx}$	m/s	Terminal velocity of particles
$\vec{v}_{air}^{ROx}$	m/s	Terminal velocity of air
$\vec{v}_{avg}^{ROx}$	m/s	Average velocity of particles and air
A_{cross}^{ROx}	m^2	Surface area of circular cross-section of a ROx pipe
t_r^{ROx}	s	Total residence time of particles in a ROx pipe
t_{ox}^{ROx}	s	Residence time for chemical energy exchange in a ROx pipe
t_{ex}^{ROx}	s	Residence time for sensible energy exchange in a ROx pipe

$$\Delta\dot{E}_{ROx} = 0 = \dot{E}_7 + \dot{E}_9 - \dot{E}_{10} - \dot{E}_{11} - \dot{E}_{18} \tag{4.0}$$

$$\dot{E}_7 = \dot{n}_p^{ROx} \cdot C_{P,p} \cdot (T_7 - T_0) + \dot{n}_p^{ROx} \cdot \frac{\delta}{2} \cdot \Delta H_{rxn} \tag{4.1}$$

$$\dot{E}_9 = \dot{n}_{air}^{ROx} \cdot C_{P,air} \cdot (T_9 - T_0) \tag{4.2}$$

$$\dot{E}_{10} = \dot{n}_{p}^{ROx} \cdot C_{P,p} \cdot (T_{10} - T_0) \tag{4.3}$$

$$\dot{E}_{11} = \dot{n}_{air}^{ROx} \cdot C_{P,air} \cdot (T_{11} - T_0) \tag{4.4}$$

$$\dot{E}_{18} = N^{pipe} \cdot \frac{\left(T_{avg}^{ROx} - T_0\right)}{R_{tot}^{ROx}} = N^{pipe} \cdot \frac{\left(T_{avg}^{ROx} - T_0\right)}{R_{h,conv}^{ROx} + R_{ins}^{ROx} + R_{c,conv}^{ROx}} \tag{4.5}$$

$$T_{avg}^{ROx} = \frac{1}{4} \cdot (T_7 + T_9 + T_{10} + T_{11}) \tag{4.6}$$

The three thermal resistance terms used to solve Eq. 4.5 are given in Eqs. 4.7 to 4.9. Equation 4.7 expresses thermal resistance for convection between air in the ROx pipe interior and the surface of the ROx pipe interior, Eq. 4.8 expresses thermal resistance for radial conduction through the insulation of the ROx pipe, and Eq. 4.9 expresses thermal resistance for convection between the surface of the ROx pipe exterior and ambient air. Contact resistance is ignored.

$$R_{h,conv}^{ROx} = \frac{1}{h_{h,ins}^{ROx} \cdot A_{h,ins}^{ROx}} \tag{4.7}$$

$$R_{ins}^{ROx} = \frac{ln\left(\frac{r_{c,ins}^{ROx}}{r_{h,ins}^{ROx}}\right)}{k_{ins}^{ROx} \cdot 2 \cdot \pi \cdot L^{pipe}} \tag{4.8}$$

$$R_{c,conv}^{ROx} = \frac{1}{h_{c,ins}^{ROx} \cdot A_{c,ins}^{ROx}} \tag{4.9}$$

The convective heat transfer coefficient in Eq. 4.7 is solved using Eqs. 4.10 to 4.12 with air properties evaluated at the film temperature expressed in Eq. 4.16 and ROx internal pressure. Equation 4.11 is an empirical relationship known as the *Dittus-Boelter equation* for internal, steady, incompressible, turbulent flow. The convection heat transfer coefficient in Eq. 4.9 is solved using Eqs. 4.13 to 4.15 with air properties evaluated at

film temperature expressed in Eq. 4.17 and pressure at ambient conditions. However, Eq. 4.12 uses a Reynolds number for a steady, incompressible flow and a Nusselt number for a fully developed turbulent flow in a smooth circular tube, while Eq. 4.15 uses a Rayleigh number for an external, free flow convection and a Nusselt number for an external free flow of a vertical plate.

$$Re_{h,ins}^{ROx} = \frac{4 \cdot \dot{m}_{air}^{pipe}}{\pi \cdot D_{h,ins}^{ROx} \cdot \mu_{air}} \tag{4.10}$$

$$Nu_{h,ins}^{ROx} = 0.023 \cdot \left(Re_{h,ins}^{ROx}\right)^{4/5} \cdot (Pr_{air})^{0.3} \tag{4.11}$$

$$h_{h,ins}^{ROx} = \frac{Nu_{h,ins}^{ROx} \cdot k_{air}}{D_{h,ins}^{ROx}} \tag{4.12}$$

$$Ra_{c,ins}^{ROx} = \frac{g \cdot \left(T_{c,ins}^{ROx} - T_0\right) \cdot \left(L^{pipe}\right)^3}{T_{f,c,ins}^{ROx} \cdot \nu_{air} \cdot \alpha_{air}} \tag{4.13}$$

$$Nu_{c,ins}^{ROx} = \left(0.825 + \frac{0.387 \cdot \left(Ra_{c,ins}^{ROx}\right)^{1/6}}{\left(1 + \left(\frac{0.492}{Pr_{air}}\right)^{9/16}\right)^{8/27}} \right)^2 \tag{4.14}$$

$$h_{c,ins}^{ROx} = \frac{Nu_{c,ins}^{ROx} \cdot k_{air}}{L^{pipe}} \tag{4.15}$$

$$T_{f,h,ins}^{ROx} = \frac{1}{2} \cdot \left(T_{h,ins}^{SR3} + T_{avg}^{ROx}\right) \tag{4.16}$$

$$T_{f,c,ins}^{ROx} = \frac{1}{2} \cdot \left(T_{c,ins}^{SR3} + T_0\right) \tag{4.17}$$

Pipe radius and surface area for one-dimensional heat transfer analysis is solved in Eqs. 4.18 to 4.21. Pipe thickness is selected as an input. Pipe diameter in Eq. 4.18 is

solved for in an iterative calculation using Eq. 4.29 with particle flow rate and ROx energy balance.

$$r_{h,ins}^{ROx} = \frac{1}{2} \cdot D_{h,ins}^{ROx} \tag{4.18}$$

$$r_{c,ins}^{ROx} = r_{h,ins}^{ROx} + t_{ins}^{ROx} \tag{4.19}$$

$$A_{h,ins}^{ROx} = 2 \cdot \pi \cdot r_{h,ins}^{ROx} \cdot L^{pipe} \tag{4.20}$$

$$A_{c,ins}^{ROx} = 2 \cdot \pi \cdot r_{c,ins}^{ROx} \cdot L^{pipe} \tag{4.21}$$

Pipe diameter in Eq. 4.29 is solved using the area of the circular cross section of the ROx pipe in Eq. 4.28 using intermediate values in Eqs. 4.22 to 4.27 for the iterative calculation. The terminal velocity of particles in the counter-current ROx pipe is solved in Eq. 4.25 for a single spherical particle. The circular cross-sectional area of the ROx pipe in Eq. 4.28 uses the terminal velocity and mass densities of the mixture of particles and air in the fluid. Air properties are evaluated at the ROx mean temperature and internal pressure.

$$A_p = \pi \cdot \left(0.5 \cdot D_p\right)^2 \tag{4.22}$$

$$V_p = \frac{4}{3} \cdot \pi \cdot \left(0.5 \cdot D_p\right)^3 \tag{4.23}$$

$$m_p = V_p \cdot \rho_p \tag{4.24}$$

$$\vec{v}_{term}^{ROx} = \left(\frac{2 \cdot m_p \cdot g}{A_p \cdot C_d \cdot \rho_{air}}\right)^{1/2} \tag{4.25}$$

$$\dot{m}_p^{pipe} = \frac{\dot{n}_p^{ROx} \cdot M_p}{N^{pipe}} \tag{4.26}$$

$$\dot{m}_{air}^{pipe} = \frac{\dot{n}_{air}^{ROx} \cdot M_{air}}{N^{pipe}} \tag{4.27}$$

$$A_{cross}^{ROx} = \frac{1}{\vec{v}_{term}^{ROx}} \cdot \left(\frac{\dot{m}_p^{pipe}}{\varrho_p^{ROx} \cdot \rho_p} + \frac{\dot{m}_{air}^{pipe}}{\left(1 - \varrho_p^{ROx}\right) \cdot \rho_{air}} \right) \tag{4.28}$$

$$D_{h,ins}^{ROx} = 2 \cdot \left(\frac{A_{cross}^{ROx}}{\pi} \right)^{1/2} \tag{4.29}$$

Pipe length in Eq. 4.34 is solved using the total residence time of particles in the pipe from Eq. 4.33 and the average velocities of the particles and air from Eq. 4.32. Residence time from Eq. 4.33 is simply the time that is required for particles to undergo full oxidation plus the time that is required for particles and air to exchange sensible energy to achieve inlet and outlet state points.

$$\vec{v}_p^{ROx} = \frac{\dot{m}_p^{pipe}}{A_{cross}^{ROx} \cdot \varrho_p^{ROx} \cdot \rho_p} \tag{4.30}$$

$$\vec{v}_{air}^{ROx} = \frac{\dot{m}_{air}^{pipe}}{A_{cross}^{ROx} \cdot (1 - \varrho_p^{ROx}) \cdot \rho_{air}} \tag{4.31}$$

$$\vec{v}_{avg}^{ROx} = \frac{\vec{v}_p^{ROx} + \vec{v}_{air}^{ROx}}{2} \tag{4.32}$$

$$t_r^{ROx} = t_{ox}^{ROx} + t_{ex}^{ROx} \tag{4.33}$$

$$L^{pipe} = t_r^{ROx} \cdot \vec{v}_{avg}^{ROx} \tag{4.34}$$

3.1.3. Equations for the Solar Receiver Reduction Reactor (SR3)

The five energy streams entering and exiting the SR3 balanced in Eq. 5.0 include the inlet particle flow (stream 1), the incoming concentrated solar flux (stream 2), the outlet particle flow (stream 4), the outlet oxygen flow (stream 5), and heat loss (stream 19). The heat loss equation for stream 19 is a combination of re-radiation losses through the SR3 aperture window and convective losses from the SR3 body. Radiation losses

from the SR3 body are ignored. Oxygen properties are evaluated at stream 5 and SR3 internal pressure.

In addition to the thermal energy streams, the SR3 has two associated auxiliary work streams: vacuum pump and particle lift. The vacuum pump lowers partial pressure of oxygen in the SR3 to further induce a reversible endothermic reaction, and uses an isothermal pump equation [43]. The particle lift conveys cold, oxidized particles to fall through the SR3 to absorb sensible heat and undergo an endothermic reaction, and uses the gravitational potential energy formula.

Table 3. Nomenclature for SR3 component variables and attributes

Nomenclature	Units	Description
$\dot{E}_{SR3}$	W	Energy balance about SR3
$\dot{E}_{19,r}$	W	Radiative losses from SR3
$\dot{E}_{19,c}$	W	Convective losses from SR3
$\dot{E}_{19,c,ins}$	W	Conductive heat transfer through SR3 insulation
$\dot{E}_{19,c,vac}$	W	Radiative heat transfer through SR3 evacuated space
$\dot{E}_{19,c,body}$	W	Conductive heat transfer through SR3 main body
$\dot{E}_{19,c,conv}$	W	Convective heat transfer from SR3 to ambient air
N_{win}	-	Number of SR3 windows
$T_{c,ins}^{SR3}$	K	Cold surface temperature of SR3 insulation
$T_{h,body}^{SR3}$	K	Hot surface temperature of SR3 main body
$T_{c,body}^{SR3}$	K	Cold surface temperature of SR3 main body
$T_{f,body}^{SR3}$	K	Film temperature between SR3 main body and ambient air
DNI	W/m^2	Direct normal solar irradiance
DNI_{dp}	W/m^2	Direct normal solar irradiance used in design point system sizing
A_1^{sf}	m^2	Area of the solar field array at solar multiple of 1
A_{SM}^{sf}	m^2	Area of the solar field array at solar multiple of SM
SM	-	Ratio of the desired solar field area to the solar field area to generate power at turbine rated capacity at the design point DNI
η_{sf}	%	Collection efficiency of the solar field
ε_{ap}	-	Emissivity of the SR3 aperture
ε_{ins}	-	Emissivity of the SR3 insulation material
ε_{body}	-	Emissivity of the SR3 main body material
A_{ap}	m^2	Total surface area of all SR3 receiver apertures

D_{win}	m	Diameter of each SR3 receiver aperture
F_{avg}	W/m^2	Average solar flux density at receiver aperture
R_{tot}^{SR3}	K/W	Total thermal resistance of SR3
R_{ins}^{SR3}	K/W	Thermal resistance of SR3 insulation conduction
R_{body}^{SR3}	K/W	Thermal resistance of SR3 main body conduction
R_{conv}^{SR3}	K/W	Thermal resistance of SR3 ambient air convection
L^{SR3}	m	Length of SR3 cavity
γ_{cav}	-	Ratio of the SR3 cavity surface area to aperture area
A_{cav}	m^2	Surface area of SR3 cylindrical cavity
$r_{c,ins}^{SR3}$	m	Radius of cold surface of SR3 insulation
$r_{h,ins}^{SR3}$	m	Radius of hot surface of SR3 insulation
$r_{c,body}^{SR3}$	m	Radius of cold surface of SR3 main body
$r_{h,body}^{SR3}$	m	Radius of hot surface of SR3 main body
t_{ins}^{SR3}	m	Thickness of SR3 insulation
t_{body}^{SR3}	m	Thickness of SR3 main body
$A_{c,body}^{SR3}$	m^2	Area for cold, radiative surface of SR3 main body
$A_{h,ins}^{SR3}$	m^2	Area for hot, radiative surface of SR3 insulation
k_{ins}^{SR3}	W/m-K	Thermal conductivity of SR3 insulation
k_{body}^{SR3}	W/m-K	Thermal conductivity of SR3 main body
Ra_{amb}^{SR3}	-	Rayleigh number of SR3 contact surface with ambient air
Nu_{amb}^{SR3}	-	Nusselt number of SR3 contact surface with ambient air
h_{amb}^{SR3}	W/m^2-K	Heat transfer coefficient of SR3 convection with ambient air

$$\Delta\dot{E}_{SR3} = 0 = \dot{E}_1 + \dot{Q}_2 - \dot{E}_4 - \dot{E}_5 - \dot{E}_{19} \tag{5.0}$$

$$\dot{E}_1 = \dot{n}_p^{SR3} \cdot C_{P,p} \cdot (T_1 - T_0) \tag{5.1}$$

$$\dot{Q}_2 = DNI \cdot A_{SM}^{sf} \cdot \eta_{sf} \tag{5.2}$$

$$\dot{E}_4 = \dot{n}_p^{SR3} \cdot C_{P,p} \cdot (T_4 - T_0) + \dot{n}_p^{SR3} \cdot \frac{\delta}{2} \cdot \Delta H_{rxn} \tag{5.3}$$

$$\dot{E}_5 = \dot{n}_{O_2}^{SR3} \cdot C_{P,O_2} \cdot (T_5 - T_0) \tag{5.4}$$

$$\dot{E}_{19} = \dot{E}_{19,r} + N_{ap} \cdot \dot{E}_{19,c} \tag{5.5}$$

$$\dot{E}_{19,r} = \sigma \cdot \varepsilon_{ap} \cdot A_{ap} \cdot T_4^4 \tag{5.6}$$

$$\dot{E}_{19,c} = \frac{T_4 - T_0}{R_{tot}^{SR3}} \tag{5.7}$$

The total thermal resistance in Eq. 5.7 is equated by balancing thermal resistance terms across each layer of the SR3 using steady-state heat loss terms that are equivalent as noted in Eq. 5.8. The four layers of insulation include conduction through insulating material (Eq. 5.9), radiation through evacuated space (Eq. 5.10), conduction through the main SR3 body material (Eq. 5.11), and convection to ambient air (Eq. 5.12).

$$\dot{E}_{19,c} = \dot{E}_{19,c,ins} = \dot{E}_{19,c,vac} = \dot{E}_{19,c,body} = \dot{E}_{19,c,conv} \tag{5.8}$$

$$\dot{E}_{19,c,ins} = \frac{T_4 - T_{c,ins}^{SR3}}{R_{ins}^{SR3}} \tag{5.9}$$

$$\dot{E}_{19,c,vac} = \frac{\sigma \cdot A_{c,ins}^{SR3} \cdot \left(\left(T_{c,ins}^{SR3}\right)^4 - \left(T_{h,body}^{SR3}\right)^4 \right)}{\frac{1}{\varepsilon_{ins}} + \left(\frac{1-\varepsilon_{body}}{\varepsilon_{body}}\right) \cdot \left(\frac{r_{c,ins}^{SR3}}{r_{h,body}^{SR3}}\right)} \tag{5.10}$$

$$\dot{E}_{19,c,body} = \frac{T_{h,body}^{SR3} - T_{c,body}^{SR3}}{R_{body}^{SR3}} \tag{5.11}$$

$$\dot{E}_{19,c,conv} = \frac{T_{c,body}^{SR3} - T_0}{R_{conv}^{SR3}} \tag{5.12}$$

The three thermal resistance terms used to solve Eqs. 5.8 to 5.12 are given in Eqs. 5.13 to 5.15. Equation 5.13 expresses thermal resistance for radial conduction through the insulation of the SR3 receiver, Eq. 5.14 expresses thermal resistance for radial conduction through the body material of the SR3 receiver, and Eq. 5.15 expresses thermal resistance for convection between the surface of the SR3 body material and ambient air.

$$R_{ins}^{SR3} = \frac{ln\left(\frac{r_{c,ins}^{SR3}}{r_{h,ins}^{SR3}}\right)}{k_{ins}^{SR3} \cdot 2 \cdot \pi \cdot L^{SR3}} \tag{5.13}$$

$$R_{body}^{SR3} = \frac{ln\left(\frac{r_{c,body}^{SR3}}{r_{h,body}^{SR3}}\right)}{k_{body}^{SR3} \cdot 2 \cdot \pi \cdot L^{SR3}} \tag{5.14}$$

$$R_{conv}^{SR3} = \frac{1}{h_{c,body}^{SR3} \cdot A_{c,body}^{SR3}} \tag{5.15}$$

The convective heat transfer coefficient for Eq. 5.15 is solved using Eqs. 5.16 to 5.18. The Rayleigh number is equated for external free convection and a Nusselt number for an external free flow of a long horizontal cylinder are used in Eq. 5.16 and Eq. 5.17, respectively. Air properties are evaluated at the film temperature expressed in Eq. 5.19 and ambient pressure.

$$Ra_{c,body}^{SR3} = \frac{g \cdot \left(T_{c,body}^{SR3} - T_0\right) \cdot \left(2 \cdot r_{body,out}^{SR3}\right)^3}{T_{f,body}^{SR3} \cdot \nu_{air} \cdot \alpha_{air}} \tag{5.16}$$

$$Nu_{c,body}^{SR3} = \left(0.6 + \frac{0.387 \cdot \left(Ra_{c,body}^{SR3}\right)^{1/6}}{\left(1 + \left(\frac{0.559}{Pr_{air}}\right)^{9/16}\right)^{8/27}} \right)^2 \tag{5.17}$$

$$h_{c,body}^{SR3} = \frac{Nu_{c,body}^{SR3} \cdot k_{air}}{2 \cdot r_{c,body}^{SR3}} \tag{5.18}$$

$$T_{f,body}^{SR3} = \frac{1}{2} \cdot \left(T_{c,body}^{SR3} + T_0\right) \tag{5.19}$$

Geometric variables including radii, length, and area dimensions for the SR3 are calculated in Eqs. 5.20 to 5.29. The required area of all apertures is calculated in Eq. 5.20. An aperture diameter is then assumed and the number of aperture windows is calculated in Eq. 5.21 with the result rounded to the nearest integer. Each window is a small opening in the cylindrical cavity of a receiver, and the cavity's surface area is sized as a multiple of a window area in Eq. 5.22 using the total aperture area, the number of windows, the ratio of insulation interior surface area to aperture area. The insulation of

the cavity interior is sized as a cylinder in Eq. 5.23 (with Eq. 3.24 thickness) that has an equivalent diameter and length. The main body exterior is also sized as a cylinder in Eq. 5.25 (with Eq. 5.26 thickness) so that view factor from the main body cylinder to the insulation cylinder is equivalent to the ratio of the circumference of a circle to the perimeter of an inscribed square.

$$A_{ap} = \frac{DNI_{dp} \cdot A_{SM}^{sf} \cdot \eta_{sf}}{F_{avg}} \tag{5.20}$$

$$N_{win} = \frac{4 \cdot A_{ap}}{\pi \cdot (D_{win})^2} \tag{5.21}$$

$$A_{cav} = (\gamma_{cav} + 1) \cdot \frac{A_{ap}}{N_{win}} \tag{5.22}$$

$$r_{h,ins}^{SR3} = \left(\frac{A_{cav}}{6 \cdot \pi}\right)^{1/2} \tag{5.23}$$

$$r_{c,ins}^{SR3} = r_{h,ins}^{SR3} + t_{ins}^{SR3} \tag{5.24}$$

$$r_{h,body}^{SR3} = \pi \cdot r_{c,ins}^{SR3} \cdot (2)^{2/3} \tag{5.25}$$

$$r_{c,body}^{SR3} = r_{h,body}^{SR3} + t_{body}^{SR3} \tag{5.26}$$

$$L^{SR3} = 2 \cdot r_{h,ins}^{SR3} \tag{5.27}$$

$$A_{c,ins}^{SR3} = 2 \cdot \pi \cdot L^{SR3} \cdot r_{c,ins}^{SR3} \tag{5.28}$$

$$A_{c,body}^{SR3} = 2 \cdot \pi \cdot L^{SR3} \cdot r_{c,body}^{SR3} \tag{5.29}$$

3.1.4. Equations for the Heat Exchanger (HX)

The five energy streams entering and exiting the HX in Eq. 6.0 include the outlet particle flow (stream 1), the outlet oxygen flow (stream 3), the inlet oxygen flow (stream 5), the inlet particle flow (stream 13), and heat loss (stream 20). Heat loss in stream 20 is

assumed to be zero. Equations 6.4 to 6.10 use the effectiveness-NTU method for a counter-flow heat exchanger to determine the outlet temperatures of the cold fluid (Eq. 6.9) and hot fluid (Eq. 6.10) with effectiveness calculated as an intermediate variable in Eq. 6.7. Oxygen properties for Eq. 6.3 is evaluated at stream 5 temperature and SR3 internal pressure.

Table 4. Nomenclature for HX component variables and attributes

Nomenclature	Units	Description
$\dot{E}_{HX}$	W	Energy balance about HX
C_c^{HX}	W/K	Heat capacity rate of HX cold fluid
C_h^{HX}	W/K	Heat capacity rate of HX hot fluid
C_{min}^{HX}	W/K	Minimum heat capacity rate of HX
C_{max}^{HX}	W/K	Maximum heat capacity rate of HX
C_r^{HX}	-	Heat capacity ratio of HX
U^{HX}	W/m^2-K	Heat transfer coefficient of HX NTU method
A^{HX}	m^2	Contact surface area of HX
NTU^{HX}	-	Number of transfer units for HX
ϵ^{HX}	-	Effectiveness of HX
Q^{HX}	W	Heat transferred between oxygen and particles

$$\Delta\dot{E}_{HX} = 0 = \dot{E}_5 + \dot{E}_{13} - \dot{E}_1 - \dot{E}_3 - \dot{E}_{20} \tag{6.0}$$

$$\dot{E}_3 = \dot{n}_{O_2}^{SR3} \cdot C_{P,O_2} \cdot (T_3 - T_0) \tag{6.1}$$

$$\dot{E}_{13} = \dot{n}_p^{SR3} \cdot C_{P,p} \cdot (T_{13} - T_0) \tag{6.2}$$

$$C_h^{HX} = \dot{n}_{O_2}^{SR3} \cdot C_{P,O_2} \tag{6.3}$$

$$C_c^{HX} = \dot{n}_p^{SR3} \cdot C_{P,p} \tag{6.4}$$

$$C_r^{HX} = \frac{C_{min}^{HX}}{C_{max}^{HX}} = \frac{min\{C_h^{ROx}, C_c^{ROx}\}}{max\{C_h^{ROx}, C_c^{ROx}\}} \tag{6.5}$$

$$NTU^{HX} = \frac{U^{HX} \cdot A^{HX}}{C_{min}^{HX}} \tag{6.6}$$

$$\epsilon^{HX} = \frac{1 - e^{-NTU^{HX} \cdot (1 - C_r^{HX})}}{1 - C_r^{HX} \cdot e^{-NTU^{HX} \cdot (1 - C_r^{HX})}} \tag{6.7}$$

$$Q^{HX} = \epsilon^{HX} \cdot C_{min}^{HX} \cdot (T_5 - T_{13}) \tag{6.8}$$

$$T_1 = T_{13} + \frac{Q^{HX}}{C_c^{HX}} \tag{6.9}$$

$$T_3 = T_5 - \frac{Q^{HX}}{C_h^{HX}} \tag{6.10}$$

3.1.5. Equations for the Hot Storage (HS)

One energy storage term and five energy streams for the HS are balanced in Eq. 7.0b. These include energy storage for the hot reduced particles mixed with inert nitrogen gas (stream 6) and energy streams including the inlet particle flow (stream 4), the outlet particle flow (stream 7), heat loss (stream 8), the inlet nitrogen flow (stream 23), and the outlet nitrogen flow (stream 23). Heat loss in Eq. 7.3 is caused by three resistances in parallel. This heat transfer problem is simplified by assuming particles and nitrogen are in thermal equilibrium, a uniform temperature throughout each media, and wall temperature inside the vessel is at the same temperature as the media in the vessel. Nitrogen property for Eq. 7.1 is evaluated at ambient temperature and ambient pressure. Nitrogen property for Eq. 7.2 is evaluated at HS internal temperature and ambient pressure.

Table 5. Nomenclature for HS component variables and attributes

Nomenclature	Units	Description
T_c^{HS}	K	Cold-surface temperature of HS
T_f^{HS}	K	Film temperature between HS and ambient air
$\dot{n}_{N,22}$	mol/s	Molar flow rate of nitrogen into HS
$\dot{n}_{N,23}$	mol/s	Molar flow rate of nitrogen exhausted from HS
$C_{P,N}$	J/mol-K	Specific heat of nitrogen

R_{tot}^{HS}	K/W	Total thermal resistance of HS
R_{up}^{HS}	K/W	Total thermal resistance through HS upper surface
$R_{up,ins}^{HS}$	K/W	Thermal resistance of HS upper surface insulation conduction
$R_{up,conv}^{HS}$	K/W	Thermal resistance of HS upper surface ambient air convection
R_{side}^{HS}	K/W	Total thermal resistance through HS radial side
$R_{side,ins}^{HS}$	K/W	Thermal resistance of HS radial side insulation conduction
$R_{side,conv}^{HS}$	K/W	Thermal resistance of HS radial side ambient air convection
R_{low}^{HS}	K/W	Total thermal resistance through HS lower surface
$R_{low,ins}^{HS}$	K/W	Thermal resistance of HS lower surface insulation conduction
$R_{low,conv}^{HS}$	K/W	Thermal resistance of HS lower surface ambient air convection
V^{HS}	m^3	Total volume of HS bin
HD^{HS}	-	Ratio of height to diameter for HS bin
H_h^{HS}	m	Total height of HS bin "hot" inner surface
H_c^{HS}	m	Total height of HS bin "cold" outer surface
r_h^{HS}	m	Radius to HS bin "hot" outer surface
r_c^{HS}	m	Radius to HS bin "cold" inner surface
D_c^{HS}	m	Diameter of HS bin "cold" inner surface
t_{ins}^{HS}	m	Thickness of HS insulation
A_h^{HS}	m^2	Surface area of HS "hot" inner upper and lower surfaces
A_c^{HS}	m^2	Surface area of HS "cold" outer upper and lower surfaces
$A_{c,side}^{HS}$	m^2	Surface area of HS "cold" inner radial surface
k_{ins}^{HS}	W/m-K	Thermal conductivity of HS insulation
Ra_{up}^{HS}	-	Rayleigh number of HS upper surface contact with ambient air
Ra_{side}^{HS}	-	Rayleigh number of HS radial surface contact with ambient air
Ra_{low}^{HS}		Rayleigh number of HS lower surface contact with ambient air
Nu_{up}^{HS}	-	Nusselt number of HS upper surface contact with ambient air
Nu_{side}^{HS}	-	Nusselt number of HS radial surface contact with ambient air
Nu_{low}^{HS}		Nusselt number of HS lower surface contact with ambient air
h_{up}^{HS}	W/m^2-K	Heat transfer coefficient of HS upper surface contact with ambient air
h_{side}^{HS}	W/m^2-K	Heat transfer coefficient of HS radial surface contact with stored nitrogen
h_{low}^{HS}	$W/m^2/K$	Heat transfer coefficient of HS lower surface contact with ambient air

$$E_{HS}^{t} = E_6^{t-1} + \Delta t \cdot \Delta \dot{E}_6 \tag{7.0a}$$

$$\Delta \dot{E}_6 = \dot{E}_6^{t-1} + \dot{E}_4^{t-1} - \dot{E}_7^{t-1} - \dot{E}_8^{t-1} + \dot{E}_{22}^{t-1} - \dot{E}_{23}^{t-1} \tag{7.0b}$$

$$\dot{E}_{22} = \dot{n}_{N,22} \cdot C_{P,N} \cdot (T_0 - T_0) = 0 \tag{7.1}$$

$$\dot{E}_{23} = \dot{n}_{N,23} \cdot C_{P,N} \cdot (T_6 - T_0) \tag{7.2}$$

$$\dot{E}_8 = \frac{T_6 - T_0}{R_{tot}^{HS}} = \frac{T_6 - T_0}{\left(\left(R_{up}^{HS}\right)^{-1} + \left(R_{side}^{HS}\right)^{-1} + \left(R_{low}^{HS}\right)^{-1}\right)^{-1}} \tag{7.3}$$

Thermal losses from hot storage in Eq. 7.3 consist of three thermal resistances in parallel: resistance through the upper surface of the hot bin from Eq. 7.4, radial resistance through the side of the hot bin from Eq. 7.5, and resistance through the lower surface of the hot bin from Eq. 7.6. Each of these resistance terms consist of two resistances in series: conductive resistance through insulation and free convection resistance to ambient air.

$$R_{up}^{HS} = R_{up,ins}^{HS} + R_{up,conv}^{HS} \tag{7.4}$$

$$R_{up,ins}^{HS} = \frac{t_{ins}^{HS}}{k_{ins}^{HS} \cdot A_h^{HS}} \tag{7.5}$$

$$R_{up,conv}^{HS} = \frac{1}{h_{up}^{HS} \cdot A_c^{HS}} \tag{7.6}$$

$$R_{side}^{HS} = R_{side,ins}^{HS} + R_{side,conv}^{HS} \tag{7.7}$$

$$R_{side,ins}^{HS} = \frac{ln\left(\frac{r_c^{HS}}{r_h^{HS}}\right)}{k_{ins}^{HS} \cdot 2 \cdot \pi \cdot H_h^{HS}} \tag{7.8}$$

$$R_{side,conv}^{HS} = \frac{1}{h_{side}^{HS} \cdot A_{c,side}^{HS}} \tag{7.9}$$

$$R_{low}^{HS} = R_{low,ins}^{HS} + R_{low,conv}^{HS} \tag{7.10}$$

$$R_{low,ins}^{HS} = \frac{t_{ins}^{HS}}{k_{ins}^{HS} \cdot A_h^{HS}} \tag{7.11}$$

$$R_{low,conv}^{HS} = \frac{1}{h_{low}^{HS} \cdot A_c^{HS}} \tag{7.12}$$

The overall heat transfer coefficient for Eqs. 7.6, 7.9, and 7.12 are solved below in Eqs. 7.15, 7.18, and 7.21, respectively. The Rayleigh numbers in Eqs. 7.13, 7.16, and 7.19 are for external, free flow fluid. The Nusselt numbers in Eq. 7.14, Eq. 7.17, and Eq. 7.20 is for the upper surface of a hot plate, the surface of a vertical plate, and the lower surface of a hot plate, respectively. The air properties for Eqs. 7.13 to 7.21 are evaluated at film temperature shown in Eq. 7.22 and ambient air pressure.

$$Ra_{up}^{HS} = \frac{g \cdot (T_c^{HS} - T_0) \cdot (D_c^{HS})^3}{T_f^{HS} \cdot \nu_{air} \cdot \alpha_{air}} \tag{7.13}$$

$$Nu_{up}^{HS} = 0.54 \cdot (Ra_{up}^{HS})^{1/4} \tag{7.14}$$

$$h_{up}^{HS} = \frac{Nu_{up}^{HS} \cdot k_{air}}{D_c^{HS}} \tag{7.15}$$

$$Ra_{side}^{HS} = \frac{g \cdot (T_c^{HS} - T_0) \cdot (H_c^{HS})^3}{T_f^{HS} \cdot \nu_{air} \cdot \alpha_{air}} \tag{7.16}$$

$$Nu_{side}^{HS} = (0.825 + \frac{0.387 \cdot (Ra_{side}^{HS})^{1/6}}{(1 + (\frac{0.492}{Pr_{air}})^{9/16})^{8/27}})^2 \tag{7.17}$$

$$h_{side}^{HS} = \frac{Nu_{side}^{HS} \cdot k_{air}}{H_c^{HS}} \tag{7.18}$$

$$Ra_{low}^{HS} = \frac{g \cdot (T_c^{HS} - T_0) \cdot (D_c^{HS})^3}{T_f^{HS} \cdot \nu_{air} \cdot \alpha_{air}} \tag{7.19}$$

$$Nu_{low}^{HS} = 0.52 \cdot (Ra_{low}^{HS})^{1/5} \tag{7.20}$$

$$h_{low}^{HS} = \frac{Nu_{low}^{HS} \cdot k_{air}}{D_c^{HS}} \tag{7.21}$$

$$T_f^{HS} = \frac{1}{2}(T_c^{HS} + T_0) \tag{7.22}$$

Geometric variables including the radii, height, area, and volume terms for the hot storage vessel are calculated in Eqs. 7.23 to 7.32. All dimensions are dependent on inputs for total number of particles in the system, the height to diameter ratio of the hot storage bin, and thickness of insulation for the hot storage bin.

$$HD^{HS} = \frac{H_h^{HS}}{2 \cdot r_h^{HS}} \tag{7.23}$$

$$V^{HS} = (1+u) \cdot \frac{N_p \cdot M_p}{\rho_p \cdot \varrho_p} \tag{7.24}$$

$$r_h^{HS} = \frac{V^{HS}}{(2 \cdot \pi \cdot HD^{HS})^{1/3}} \tag{7.25}$$

$$r_c^{HS} = r_h^{HS} + t_{ins}^{HS} \tag{7.26}$$

$$D_c^{HS} = 2 \cdot r_c^{HS} \tag{7.27}$$

$$H_h^{HS} = \frac{V^{HS}}{\pi \cdot (r_h^{HS})^2} \tag{7.28}$$

$$H_c^{HS} = H_h^{HS} + 2 \cdot t_{ins}^{HS} \tag{7.29}$$

$$A_h^{HS} = \pi \cdot (r_h^{HS})^2 \tag{7.30}$$

$$A_c^{HS} = \pi \cdot (r_c^{HS})^2 \tag{7.31}$$

$$A_{c,side}^{HS} = \pi \cdot D_c^{HS} \cdot H_c^{HS} \tag{7.32}$$

3.1.6. Equations for the Cold Storage (CS)

One energy storage term and five energy streams for the CS are balanced in Eq. 8.0b. These include energy storage for the cold oxidized particles mixed with ambient air (stream 12) and energy streams including the inlet particle flow (stream 10), the outlet particle flow (stream 13), heat loss (stream 14), the inlet air flow (stream 24), and the

outlet air flow (stream 25). Heat loss in Eq. 8.3 is caused by three resistances in parallel. This heat transfer problem is simplified by assuming particles and air are in thermal equilibrium, a uniform temperature throughout each media, and wall temperature inside the vessel is at the same temperature as the media in the vessel. Air property for Eq. 8.1 is evaluated at ambient temperature and ambient pressure. Air property for Eq. 8.2 is evaluated at CS internal temperature and ambient pressure.

Table 6. Nomenclature for CS component variables and attributes

Nomenclature	Units	Description
T_c^{CS}	K	Cold-surface temperature of CS
T_f^{CS}	K	Film temperature between CS and ambient air
$\dot{n}_{air,24}$	mol/s	Molar flow rate of nitrogen into CS
$\dot{n}_{air,25}$	mol/s	Molar flow rate of nitrogen exhausted from CS
R_{tot}^{CS}	K/W	Total thermal resistance of CS
R_{up}^{CS}	K/W	Total thermal resistance through CS upper surface
$R_{up,ins}^{CS}$	K/W	Thermal resistance of CS upper surface insulation conduction
$R_{up,conv}^{CS}$	K/W	Thermal resistance of CS upper surface ambient air convection
R_{side}^{CS}	K/W	Total thermal resistance through CS radial side
$R_{side,ins}^{CS}$	K/W	Thermal resistance of CS radial side insulation conduction
$R_{side,conv}^{CS}$	K/W	Thermal resistance of CS radial side ambient air convection
R_{low}^{CS}	K/W	Total thermal resistance through CS lower surface
$R_{low,ins}^{CS}$	K/W	Thermal resistance of CS lower surface insulation conduction
$R_{low,conv}^{CS}$	K/W	Thermal resistance of CS lower surface ambient air convection
V^{CS}	m^3	Total volume of CS bin
HD^{CS}	-	Ratio of height to diameter for CS bin
H_h^{CS}	m	Total height of CS bin “hot” inner surface
H_c^{CS}	m	Total height of CS bin “cold” outer surface
r_h^{CS}	m	Radius to CS bin “hot” outer surface
r_c^{CS}	m	Radius to CS bin “cold” inner surface
D_c^{CS}	m	Diameter of CS bin “cold” inner surface
t_{ins}^{CS}	m	Thickness of CS insulation
A_h^{CS}	m^2	Surface area of CS “hot” inner upper and lower surfaces
A_c^{CS}	m^2	Surface area of CS “cold” outer upper and lower surfaces
$A_{c,side}^{CS}$	m^2	Surface area of CS “cold” inner radial surface
k_{ins}^{CS}	W/m-K	Thermal conductivity of CS insulation
Ra_{up}^{CS}	-	Rayleigh number of CS upper surface contact with ambient air
Ra_{side}^{CS}	-	Rayleigh number of CS radial surface contact with ambient air

Ra_{low}^{CS}		Rayleigh number of CS lower surface contact with ambient air
Nu_{up}^{CS}	-	Nusselt number of CS upper surface contact with ambient air
Nu_{side}^{CS}	-	Nusselt number of CS radial surface contact with ambient air
Nu_{low}^{CS}		Nusselt number of CS lower surface contact with ambient air
h_{up}^{CS}	W/m^2-K	Heat transfer coefficient of CS upper surface contact with ambient air
h_{side}^{CS}	W/m^2-K	Heat transfer coefficient of CS radial surface contact with stored nitrogen
h_{low}^{CS}	W/m^2/K	Heat transfer coefficient of CS lower surface contact with ambient air

$$E_{CS}^{t} = E_{12}^{t-1} + \Delta t \cdot \Delta \dot{E}_{12} \tag{8.0a}$$

$$\Delta \dot{E}_{12} = \dot{E}_{12}^{t-1} + \dot{E}_{10}^{t-1} - \dot{E}_{13}^{t-1} - \dot{E}_{14}^{t-1} + \dot{E}_{24}^{t-1} - \dot{E}_{25}^{t-1} \tag{8.0b}$$

$$\dot{E}_{24} = \dot{n}_{air,24} \cdot C_{P,air} \cdot (T_0 - T_0) = 0 \tag{8.1}$$

$$\dot{E}_{25} = \dot{n}_{air,25} \cdot C_{P,air} \cdot (T_{12} - T_0) \tag{8.2}$$

$$\dot{E}_{14} = \frac{T_{12} - T_0}{R_{tot}^{CS}} = \frac{T_{12} - T_0}{\left(\left(R_{up}^{CS}\right)^{-1} + \left(R_{side}^{CS}\right)^{-1} + (R_{low}^{CS})^{-1}\right)^{-1}} \tag{8.3}$$

Thermal losses from cold storage in Eq. 8.3 consist of three thermal resistances in parallel: resistance through the upper surface of the cold bin from Eq.1 6.4, radial resistance through the side of the cold bin from Eq. 8.5, and resistance through the lower surface of the cold bin from Eq. 8.6. Each of these resistance terms consist of two resistances in series: conductive resistance through insulation and free convection resistance to ambient air.

$$R_{up}^{CS} = R_{up,ins}^{CS} + R_{up,conv}^{CS} \tag{8.4}$$

$$R_{up,ins}^{CS} = \frac{t_{ins}^{CS}}{k_{ins}^{CS} \cdot A_h^{CS}} \tag{8.5}$$

$$R_{up,conv}^{CS} = \frac{1}{h_{up}^{CS} \cdot A_c^{CS}} \tag{8.6}$$

$$R_{side}^{CS} = R_{side,ins}^{CS} + R_{side,conv}^{CS} \tag{8.7}$$

$$R_{side,ins}^{CS} = \frac{ln\left(\frac{r_c^{CS}}{r_h^{CS}}\right)}{k_{ins}^{CS} \cdot 2 \cdot \pi \cdot H_h^{CS}} \tag{8.8}$$

$$R_{side,conv}^{CS} = \frac{1}{h_{side}^{CS} \cdot A_{c,side}^{CS}} \tag{8.9}$$

$$R_{low}^{CS} = R_{low,ins}^{CS} + R_{low,conv}^{CS} \tag{8.10}$$

$$R_{low,ins}^{CS} = \frac{t_{ins}^{CS}}{k_{ins}^{CS} \cdot A_h^{CS}} \tag{8.11}$$

$$R_{low,conv}^{CS} = \frac{1}{h_{low}^{CS} \cdot A_c^{CS}} \tag{8.12}$$

The overall heat transfer coefficient for Eqs. 8.6, 8.9, and 8.12 are solved below in Eqs. 8.15, 8.18, and 8.21, respectively. The Rayleigh numbers in Eqs. 8.13, 8.16, and 8.19 are for external, free flow fluid. The Nusselt numbers in Eq. 8.14, Eq. 8.17, and Eq. 8.20 is for the upper surface of a hot plate, the surface of a vertical plate, and the lower surface of a hot plate, respectively. The air properties for Eqs. 8.13 to 8.21 are evaluated at film temperature shown in Eq. 8.22 and ambient air pressure.

$$Ra_{up}^{CS} = \frac{g \cdot (T_c^{CS} - T_0) \cdot (D_c^{CS})^3}{T_f^{CS} \cdot \nu_{air} \cdot \alpha_{air}} \tag{8.13}$$

$$Nu_{up}^{CS} = 0.54 \cdot (Ra_{up}^{CS})^{1/4} \tag{8.14}$$

$$h_{up}^{CS} = \frac{Nu_{up}^{CS} \cdot k_{air}}{D_c^{CS}} \tag{8.15}$$

$$Ra_{side}^{CS} = \frac{g \cdot (T_c^{CS} - T_0) \cdot (H_c^{CS})^3}{T_f^{CS} \cdot \nu_{air} \cdot \alpha_{air}} \tag{8.16}$$

$$Nu_{side}^{CS} = (0.825 + \frac{0.387 \cdot (Ra_{side}^{CS})^{1/6}}{(1 + (\frac{0.492}{Pr_{air}})^{9/16})^{8/27}})^2 \tag{8.17}$$

$$h_{side}^{CS} = \frac{Nu_{side}^{CS} \cdot k_{air}}{H_c^{CS}} \tag{8.18}$$

$$Ra_{low}^{CS} = \frac{g \cdot (T_c^{CS} - T_0) \cdot (D_c^{CS})^3}{T_f^{CS} \cdot \nu_{air} \cdot \alpha_{air}} \tag{8.19}$$

$$Nu_{low}^{CS} = 0.52 \cdot (Ra_{low}^{CS})^{1/5} \tag{8.20}$$

$$h_{low}^{CS} = \frac{Nu_{low}^{CS} \cdot k_{air}}{D_c^{CS}} \tag{8.21}$$

$$T_f^{CS} = \frac{1}{2}(T_c^{CS} + T_0) \tag{8.22}$$

Geometric variables including the radii, height, and area terms for the cold storage vessel are calculated in Eqs. 8.23 to 8.32. All dimensions are dependent on inputs for the total number of particles in the system, the height to diameter ratio of the cold storage bin, and thickness of insulation for the cold storage bin.

$$HD^{CS} = \frac{H_h^{CS}}{2 \cdot r_h^{CS}} \tag{8.23}$$

$$V^{CS} = (1 + u) \cdot \frac{N_p \cdot M_p}{\rho_p \cdot \varrho_p} \tag{8.24}$$

$$r_h^{CS} = \frac{V^{CS}}{(2 \cdot \pi \cdot HD^{CS})^{1/3}} \tag{8.25}$$

$$r_c^{CS} = r_h^{CS} + t_{ins}^{CS} \tag{8.26}$$

$$D_c^{CS} = 2 \cdot r_c^{CS} \tag{8.27}$$

$$H_h^{CS} = \frac{V^{CS}}{\pi \cdot (r_h^{CS})^2} \tag{8.28}$$

$$H_c^{CS} = H_h^{CS} + 2 \cdot t_{ins}^{CS} \tag{8.29}$$

$$A_h^{CS} = \pi \cdot (r_h^{CS})^2 \tag{8.30}$$

$$A_c^{CS} = \pi \cdot (r_c^{CS})^2 \tag{8.31}$$

$$A_{c,side}^{CS} = \pi \cdot D_c^{CS} \cdot H_c^{CS} \tag{8.32}$$

3.1.7. Calculating states for the Power Block

A one-dimensional steady state quasi-equilibrium Engineering Equation Solver (EES) model was developed for the air Brayton cycle using the Ansaldo Energia AE64.3A gas turbine to calculate unknown state information needed for the PROMOTES model. The AE64.3A gas turbine capacity of 75 MWe provides a base configuration that can include a bottoming Rankine cycle for a total of 111.7 MWe. The primary values of interest obtained from the EES model include the compressor air outlet temperature and the turbine air inlet temperature. These correspond to the ROx air inlet temperature and ROx air outlet temperature, respectively. The vendor provided values shouldn't vary between gas-only and combined cycle configurations.

Table 7. Ansaldo Energia AE64.3A EES model inputs and outputs

Parameter Description	Manufacturer Value	PROMOTES Value
Gas turbine capacity	75 MW	75 MW
Combined cycle capacity	111.7 MW	111.7 MW
Combustor heat rate	-	208.9 MW
Gas turbine efficiency	35.9%	35.9%
Combined cycle efficiency	-	53.5%
Compressor isentropic efficiency	-	96.3%
Turbine isentropic efficiency	-	78.9%
Combustor efficiency	-	94.1%
Air mass flow rate	213 kg/s	213 kg/s
Compression ratio	16.7	16.7
Compressor air inlet pressure	101 kPa	101 kPa
Compressor air inlet temperature	15 C	15 C
Compressor air outlet temperature	-	383 C
Turbine air inlet temperature	1190 C	1200 C
Turbine air outlet temperature	574 C	574 C

Table 7 provides a list of known manufacturer values and the unknown values that were calculated. The combustor heat rate term is solved using combined cycle capacity and efficiency. Compressor and turbine isentropic efficiency values were solved using state values, pressure ratio, and energy balance for the known electrical power output. Compressor air inlet temperature is per ISO conditions. The turbine inlet temperature (TIT), by definition, is less than or equal to TIT_{ISO}, allowing the use of a slightly higher value than the manufacturer provided. The model assumes no pressure loss in piping or across combustor, and that the compressor and turbine are both adiabatic and isentropic.

3.2. Simulation & Analysis

The simulation and analysis process is conducted in four stages to equate multiple intermediate and dependent variables. Stage 1 calculates component sizes including the surface contact area between the particles and oxygen in the heat exchanger, the dimensions of the multi-tubular pipes that compose the ROx reactor, and volume of the storage bins to achieve desired off-sun capacity (six-hours is nominal). Stage 2 performs time series simulation of the input system design and test conditions using data computed from the first stage. Stage 3 computes performance characteristics—e.g., energy efficiency, capacity factor—and other results of the time series simulation. Stage 4 is the sensitivity analysis of system and component variables on system performance characteristics.

Stage 1: Component sizing

Heat exchanger component: Select design point irradiance (DNI_{dp}) and the lowest expected temperature for HX inlet particle temperature (T_{13}) to solve for the heat capacity rates of the inlet particle and oxygen fluids at design point. Set the input value for oxygen-particle heat transfer coefficient (U^{HX}) so that the NTU^{HX} parameter only varies based on heat exchanger contact area (A^{HX}). Solve for A^{HX} such that the desired heat transfer effectiveness is reached (ϵ^{HX}).

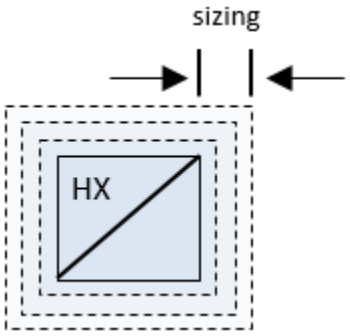

Figure 3. The HX surface area is sized as a function of effectiveness and heat transfer coefficient

Re-oxidizer reactor: Select lowest excepted temperature for ROx particle inlet temperature (T_7). Select an initial particle molar flow rate ($\dot{n}_p^{ROx}$), then solve for the average velocity of the particles with respect to air ($\vec{v}_{avg}^{ROx}$), and the diameter of ROx pipe ($D_{h,ins}^{ROx}$). Use $\vec{v}_{avg}^{ROx}$ and the total residence time of particles in the pipe (t_r^{ROx}) to solve for the length of the ROx pipe (L^{pipe}). Use the ROx energy balance to calculate the expected particle molar flow rate ($\dot{n}_p^{ROx}$); if this term and the initial particle flow rate are different, then repeat this process with the expected particle molar flow rate. Continue until $\dot{n}_p^{ROx}$ converges, producing the desired $D_{h,ins}^{ROx}$.

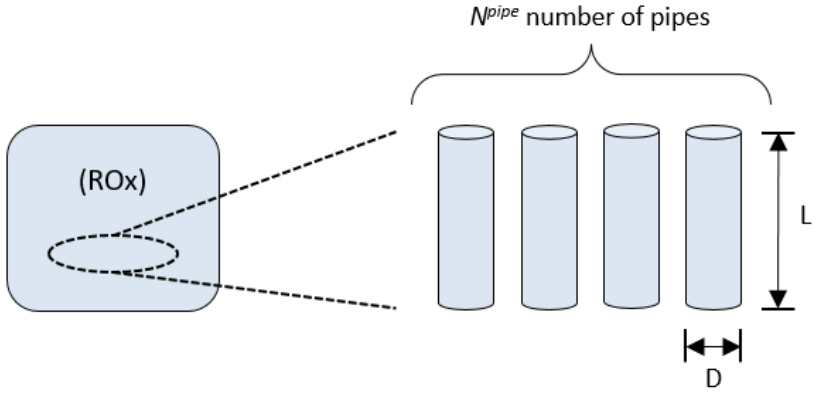

Figure 4. The dimensions of the ROx pipes depend on particle flow rate and average terminal velocity of the particles with respect to air
Does not indicate actual arrangement of ROx pipes during installation

Hot storage and cold storage bins: Use the final $\dot{n}_p^{ROx}$ term from the ROx pipe sizing above to calculate the number of particle mols (N_p) needed to achieve desired off-sun storage capacity. Solve for V^{HS} and V^{CS}.

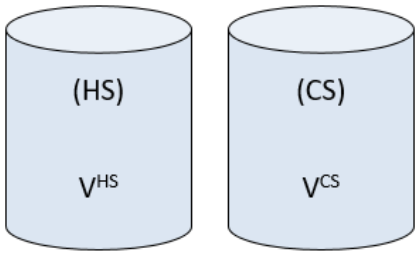

Figure 5. The volume of the storage bins depends on the amount of particles for off-sun generation

Stage 2: Time series simulation

Time series simulation occurs through a series of hourly energy stream balances that depends on operating state, solar availability, and particle availability in the hot or cold bin. Figure 6 summarizes the 10-step simulation process from beginning time index $i = 1$ to ending time index $i = 8760$. Prior to executing the time series simulation, two initializing steps need to be performed. *Step one* and *step two* solve for extent of reduction (δ) and set the time index to the first hour of the day, respectively. *Step three*

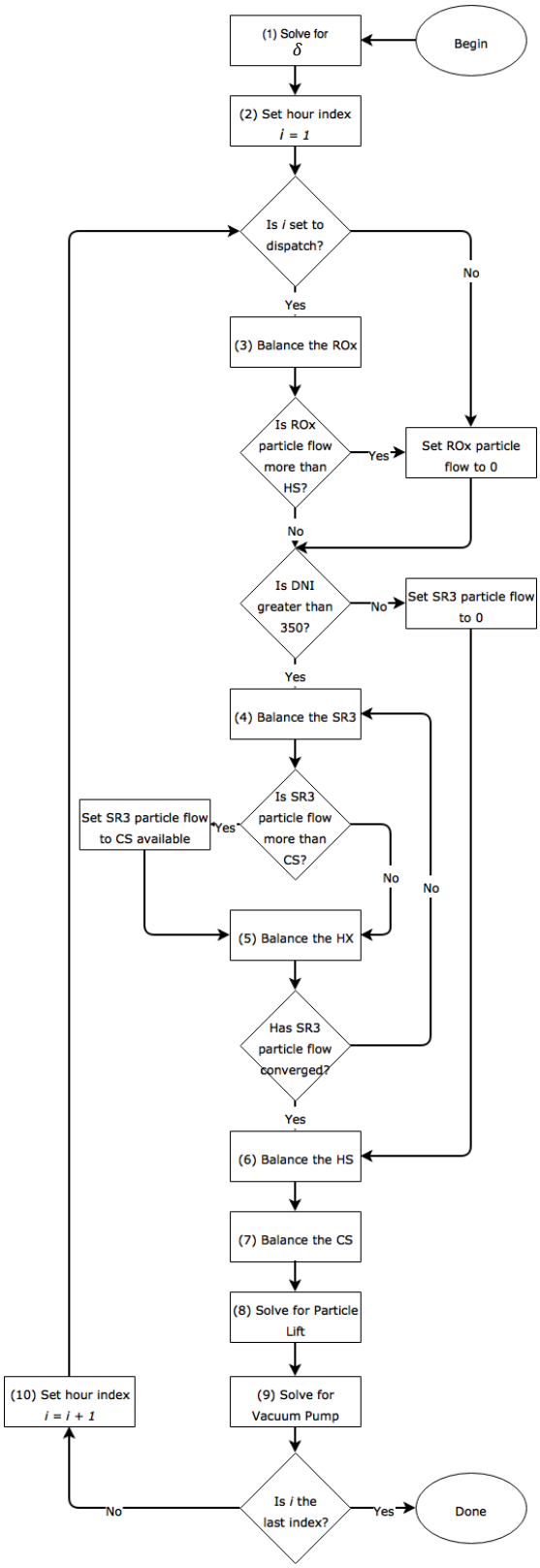

Figure 6. The PROMOTES time series simulation process

balances the ROx reactor energy stream to output the molar flow rate of particles ($\dot{n}_p^{ROx}$) through the ROx if the current time index is set to dispatch power and if HS contains enough particles for one hour of generation. *Step four* balances the SR3 energy stream to output the molar flow rate of particles ($\dot{n}_p^{SR3}$) and oxygen ($\dot{n}_{O_2}^{SR3}$) through the SR3 if the DNI incident on the solar field exceeds the minimum operating irradiance of 350 W/m^2 (300 is used elsewhere [44]) and if $\dot{n}_p^{SR3}$ over the time step does not exceed what's dischargeable from cold storage and what's immediately available from $\dot{n}_p^{ROx}$ over the time step. If solar field is greater than 350 W/m^2 but $\dot{n}_p^{SR3}$ had to be reduced, then this loss is considered spillage losses. *Step five* balances the HX by using step four's output $\dot{n}_p^{SR3}$ and $\dot{n}_{O_2}^{SR3}$ to solve for the outlet particle (T_1) and oxygen (T_3) temperatures, respectively. Step four and five are interdependent, therefore

they are run in a loop until the output for $\dot{n}_p^{SR3}$ converges. *Step six* balances the HS energy and mass streams by using $\dot{n}_p^{SR3}$ and $\dot{n}_p^{ROx}$ to charge (fill) and discharge (empty), respectively, the hot storage bin and update internal temperature (T_6). *Step seven* balances the CS energy and mass streams by using $\dot{n}_p^{SR3}$ and $\dot{n}_p^{ROx}$ to discharge (fill) and charge (empty), respectively, the cold storage bin and update internal temperature (T_{12}). *Step eight* and *step nine* use $\dot{n}_p^{SR3}$ and $\dot{n}_{O_2}^{SR3}$, respectively, to calculate work input into the PROMOTES subsystem boundary. *Step ten* increments the time series simulation to the next hour until completion of all hours.

Stage 3: Performance characteristics:

After the completion of stage 2's time series simulation, the resulting hourly system states for the day are used to measure system performance metrics. Two system performance metrics are evaluated in stage 3, the annual system energy efficiency and the annual capacity factor. These performance metrics are defined in Eqs. 9.3 and 9.4, while the general definition of these metrics are defined in Eqs. 9.0 and 9.1, below.

Equation 9.0 provides the general definition of energy efficiency as the ratio of useful energy output to the energy input. Equation 9.1 provides the general definition of capacity factor as the ratio of actual plant generation to the maximum potential plant generation at rated power, which is number between 0 (worst) and 1 (best) that indicates plant productivity and utilization.

$$\eta_E = \frac{E_{useful}}{E_{in}} \tag{9.0}$$

$$CF = \frac{G_{actual}}{G_{rated}} \tag{9.1}$$

Table 8 lists the 2 performance metrics used to assess system-wide performance. Eleven energy streams that are uniquely calculated for every hourly time step i of the time series simulation are used to calculate these metrics. The tower thermal subsystem boundary begins at the solar thermal energy entering the SR3 and ends at the thermal energy transferred from the ROx to the air Brayton turbine. The energy stream terms here are not rates because the storage terms are tracked in Joules and not Watts, therefore the power terms (W) are converted to energy terms (J) by scaling with time step Δt.

Table 8. Performance metrics

Figure of Merit	Units	Description
$\eta_{E,sys}$	%	Annual system energy efficiency
CF_{sys}	%	Annual system capacity factor

Equations 9.2 to 9.4 below use the definition of energy efficiency shown in Eq. 9.0 and the definition of capacity factor shown in Eq. 9.1. The ROx energy efficiency definition in Eq. 9.2 only considers thermal losses through the insulation. Other loss terms that are not included in this model, since the ROx replaces the turbine combustor, are pressure drop and mass loss in the air stream. Equation 9.3 shows that the annual system energy efficiency is the product of the solar collection field, tower thermal, auxiliary loads, and power block energy efficiencies. The tower thermal energy efficiency depends on the net energy stream from the ROx to the air Brayton turbine, the sum of all solar thermal energy entering the SR3 component, the change in energy storage from beginning hourly time index $i = 1$ to ending hourly time index $i = 8760$, and the energy efficiency of the ROx component from Eq. 9.2. The auxiliary load

subsystem energy efficiency is reduced by the ratio of electric power required to operate the particle lift and vacuum pump to the amount of power generated by the power block.

$$\eta_{E,ROx} = \frac{\sum_{i=1}^{8760}\left(E_{11}^{i} - E_{9}^{i}\right)}{\sum_{i=1}^{8760}\left(E_{7}^{i} - E_{10}^{i}\right)} \tag{9.2}$$

$$\eta_{E,sys} = \eta_{sf} \cdot \left(\frac{\sum_{i=1}^{8760}\left(E_{11}^{i} - E_{9}^{i}\right) + \eta_{E,ROx} \cdot E_{HS}^{8760} + E_{CS}^{8760}}{\sum_{i=1}^{8760}\left(E_{2}^{i}\right) + \eta_{E,ROx} \cdot E_{HS}^{1} + E_{CS}^{1}}\right) \cdot \left(1 - \frac{\sum_{i=1}^{8760}\left(E_{15}^{i} + E_{16}^{i}\right)}{\sum_{i=1}^{8760}\left(G^{i}\right)}\right) \cdot \eta_{E,cc} \tag{9.3}$$

Equation 9.4 is the definition of annual capacity factor. It is the summation of gross amount of power generated for the year divided by the maximum amount of power that can be generated for the year.

$$CF_{sys} = \frac{\sum_{i=1}^{8760}\left(G^{i}\right)}{8760 \cdot G_{rated}} \tag{9.4}$$

Stage 4: Sensitivity analysis:

Table 9 shows the eleven chosen sensitivity variables used to perform a sensitivity analysis on particle extent of reduction (δ), particle energy density, storage bin sizing, annual system energy density, and annual system capacity factor. Extent of reduction is analyzed by varying internal SR3 temperature and partial pressure of oxygen in the SR3 (defined in section 3.1.1), and the energy density of the particles as analyzed by varying δ and enthalpy of reduction, ΔH_{rxn}. The sizing of the HS and CS bins is analyzed as a function of extent of reduction and number of storage hours. The two system-wide performance metrics considered are the annual system-wide capacity factor and energy efficiency metrics. Capacity factor is analyzed as a function of solar multiple and number of storage hours. System energy efficiency is analyzed in terms of eight component

parameters that include the solar multiple, δ, heat exchanger contact area, and the thickness of five component materials.

Table 9. System and component sensitivity variables

Dependent Output	System or Component	Sensitivity Variable
δ	SR3	T_4
δ	SR3	$P_{O_2}^{SR3}$
Particle energy density	Particles	δ
Particle energy density	Particles	ΔH_{xn}
Mass of particles in storage	Particles	δ
Mass of particles in storage	HS and CS	Storage hours
CF_{sys}	Solar field	SM
CF_{sys}	HS and CS	Storage hours
$\eta_{E,sys}$	Solar field	SM
$\eta_{E,sys}$	Particles	δ
$\eta_{E,sys}$	HX	A^{HX}
$\eta_{E,sys}$	ROx	t_{ins}^{ROx}
$\eta_{E,sys}$	SR3	t_{ins}^{SR3}
$\eta_{E,sys}$	SR3	t_{body}^{SR3}
$\eta_{E,sys}$	HS	t_{ins}^{HS}
$\eta_{E,sys}$	CS	t_{ins}^{CS}

3.3. Model Input Data

Table 10 provides a detailed list of the sixty-seven system-wide and component specific input values. Six temperature states in Table 10, which include T_1, T_3, T_6, T_7, T_{12}, and T_{13}, vary every time step based on system conditions and component performance. For instance, T_1 and T_3 are values output by the HX that change every time step because it is dependent on the effectiveness of the NTU heat transfer equation, which depends on capacitances that vary. The input value for this varying temperature states is set as the initial condition. Refer to the expanded and complete tables throughout section 3.1 for a detailed list of all input, intermediate, and output variables.

The particle taken here is CAM28, $CaAl_{0.2}Mn_{0.8}O_{2.9}$, with appropriate molar mass (M_p), density (ρ_p), and enthalpy of reduction reaction (ΔH_{rxn}). The drag coefficient (C_d) and packing density in storage (ϱ_p) is set to the equivalent of a sphere [45, 46]. The 5 material thicknesses are based on internal designs, and analyzed as sensitivity variables.

The air inlet (T_9) and outlet (T_{11}) temperature states about the ROx correspond to the turbine compressor outlet and turbine inlet temperatures, respectively, and are calculated from the internal AE64.3A thermodynamic EES model by validating against manufacturer data as boundary conditions. The internal pressure (P_{comp}^{ROx}) and air mass flow rate ($\dot{n}_{air}^{ROx}$) for the ROx are directly available from manufacturer data [47]. The total residence time of particles in the ROx pipe (t_r^{ROx}) is simplified by splitting the process into two stages, the time for re-oxidation of particles (t_{ox}^{ROx}) near the particle inlet and the time for sensible energy exchange (t_{ex}^{ROx}) to achieve ROx boundary states. The former is expected to occur on the order of seconds and is taken here to be 1 second [48], the latter is approximated as 3 seconds using an internal discretized lumped capacitance model, for a single particle, of the transience of sensible energy exchange in 1 °K increments.

The average collector efficiency, from incident solar radiation on the heliostat mirrors to concentrated radiation entering the receiver aperture, can range from 52% to 64%, which we take for the purposes here as a simplifying constant 60% [49, 50]. The SR3 has three radiative surfaces modeled using emissivity terms. The emissivity of the receiver window and the insulation layer is set to 0.95 of block body efficiency and 0.8 for silica RSLE-57 [51], respectively, and the emissivity of the 304 stainless steel body, which can range from 0.36 to 0.73 at high temperatures, is set to 0.7 [52].

Table 10. Input values for systems-wide and component attributes

System or Component(s)	Term	Value	Units
System-wide	Δt	3600	s
System-wide	T_0	298.15	K
HX to SR3	T_1	527.15	K
HX	T_3	473.15	K
SR3 to HS	T_4	1,323.15	K
SR3 to HX	T_5	1,323.15	K
HS	T_6	1,319.15	K
HS to ROx	T_7	1,319.15	K
Air Brayton to ROx	T_9	656.15	K
ROx to CS	T_{10}	663.15	K
ROx to air Brayton	T_{11}	1,473.15	K
CS	T_{12}	661.15	K
CS to HX	T_{13}	661.15	K
Air Brayton	T_{20}	288.15	K
Air Brayton	T_{21}	847.15	K
System-wide	P_0	101,325.00	Pa
System-wide	P_{O_2}	2,127.00	Pa
SR3	$P_{O_2}^{SR3}$	200.00	Pa
System-wide	N_p	37,848,000	mol
Particle	M_p	135.82	g/mol
Particle	M_{air}	28.97	g/mol
Particle	ρ_p	3,942.03	kg/m^3
Particle	$C_{P,p}$	125.91	J/mol-K
Particle	ΔH_{rxn}	320,000	J/mol-O_2
System-wide	R	8.314	J/mol-K
System-wide	σ	5.67×10^{-8}	W/m^2-K^4
System-wide	g	9.81	m/s^2
Particle lift	H_{lift}	135	m
Particle lift	η_{lift}	80	%
Particle lift	$Load_{lift}$	5,000	W
Vacuum pump	η_{pump}	40	%
Vacuum pump	$Load_{pump}$	86,800	W
ROx	N^{pipe}	23	-
ROx	P_{comp}^{ROx}	1,692,127.50	Pa
ROx	$\dot{n}_{air}^{ROx}$	7,344.83	mol/s
ROx	L^{pipe}	4.248	m
ROx	$D_{h,ins}^{ROx}$	1.028	m
ROx	t_{ins}^{ROx}	0.076	m
ROx	k_{ins}^{ROx}	0.750	W/m-K
Particle	D_p	0.00025	m
Particle	C_d	0.50	-

ROx	ϱ_p^{ROx}	5	%
ROx	t_r^{ROx}	4	s
ROx	t_{ox}^{ROx}	1	s
ROx	t_{ex}^{ROx}	3	s
SR3	DNI_{dp}	900	W/m^2
SR3	A_1^{sf}	432,410	m^2
SR3	SM	1.8	-
SR3	η_{sf}	60	%
SR3	ε_{ap}	0.95	-
SR3	ε_{ins}	0.80	-
SR3	ε_{body}	0.70	-
SR3	D_{win}	1.00	m
SR3	F_{avg}	2,000,000	W/m^2
SR3	γ_{cav}	16	-
SR3	t_{ins}^{SR3}	0.0381	m
SR3	t_{body}^{SR3}	0.0254	m
SR3	k_{ins}^{SR3}	0.75	W/m-K
SR3	k_{body}^{SR3}	16.00	W/m-K
HX	U^{HX}	12	W/m^2-K
HX	A^{HX}	1042	m^2
HS and CS	u	10	%
HS and CS	ϱ_p	65	%
HS	HD^{HS}	1.5	-
HS	t_{ins}^{HS}	0.715	m
HS	k_{ins}^{HS}	0.50	W/m-K
CS	HD^{CS}	1.50	-
CS	t_{ins}^{CS}	0.715	m
CS	k_{ins}^{CS}	0.50	W/m-K
Power block	$\eta_{E,cc}$	53.50	%

The thermal circuit model results depend largely on the thickness and thermal conductivity of the insulating materials. The ROx and SR3 here use RSLE-57 as insulation material, which has a thermal conductivity of 0.75 W/m-K [53]. The SR3 has an additional conductivity layer, the 304 stainless steel body which has a thermal conductivity of 16 W/m-K [54]. The HS and CS are constructed using the same materials, firebrick, perlite concrete, and reinforced concreted which have thermal conductivity values at high temperatures ranging from 0.21-0.57 W/m-K, 0.54-0.83 W/m-K, and 0.99-

1.10 W/m-K, respectively [55, 56, 57]. An overall thermal conductivity value for the HS and CS is assumed to be 0.5 W/m-K.

The heat exchanger that recovers thermal energy from the hot oxygen exhaust uses an overall heat transfer coefficient value (U^{HX}) of 12 W/m^2-K for gas-to-gas inside and outside tubes [58]. The mechanical work-to-electricity efficiency of the particle lift (η_{lift}) is set to 80%, similar to that achieved by mine hoists [59], and the work-to-electricity efficiency of the vacuum pump (η_{pump}) is approximated as 40% [43].

Yearly solar irradiance data are used to perform time series simulations. The solar irradiance profile used here is TMY3 DNI measurements for Barstow, CA [60]. Three days of the year from the Barstow data set is used to represent each season's typical solar performance and are chosen because their daily irradiance profiles are within 0.5% of the seasonal averages. The medium solar seasons of spring and autumn are represented by April 17, the high solar season of summer is represented by July 19, and the low solar season of winter is represented by March 12. Table 11 summarizes these daily profiles.

Table 11. Barstow, CA solar DNI summary statistics for the three days of the year

Case Study Day	Day of Year	Daily Irradiance
Summer (high)	June 14	9.206 kWh/m^2/day
Spring and Autumn (medium)	April 17	7.579 kWh/m^2/day
Winter (low)	March 12	5.474 kWh/m^2/day

4. RESULTS

Results for the 111.7 MWe system operation under three case study days using the Barstow DNI data set are shown in Figs. 7, 8, and 9. These three days were used to profile plant operation, productivity, and spillage for high (summer), medium (spring and autumn), and low (winter) solar periods of the year. Each dispatch schedule was required to store enough reduced particles to generate electric power for six off-sun hours. Figures 7, 8, and 9 begin off-sun dispatch immediately after sunset. This is an idealized off-sun dispatch schedule, because, under actual operation, off-sun dispatch can occur anytime between sunset and sunrise, and any particles kept in storage (dispatched closer to sunrise) will lose more sensible energy.

The intraday profile figures have two axes: on the left is the rate at which particles are flowing through the SR3 and ROx components, and on the right is the amount of particles stored in the HS and CS bins. The rate at which particles are flowing through the SR3 (capturing solar energy) is shown as a white line, and the rate at which the particles are flowing through the ROx (releasing solar energy) is shown as the blue line (dispatching enough for rated power or none at all). The amount of particles stored in CS are represented by the black shaded area, in contrast to the amount of stored particles in HS, which are represented by the orange shaded area. Thus, as hot storage charges (orange), the cold storage similarly discharges (black). The current model, to simplify, only dispatches in hourly intervals (111.7 MWe) and targets a dispatch schedule for six hours-off sun generation. Alternative dispatch schedules—e.g. dispatching in sub-hourly intervals—was examined offline and can generate more energy by minimizing storage spillage. These alternative productivity schedules are represented below as green bars,

and correspond to the ROx particle flow rate (blue line) but generate power for a fraction of an additional hour.

Figure 7 shows the spring (equivalent to autumn) equinox case study (medium solar). The particles began flowing through the SR3 during the 7th hour, stopped momentarily during the 8th hour, and completely stopped flowing during the 17th hour. The power block generated on-sun power between the 11th and 17th hours, and generated off-sun power between the 19th and 24th hours. The HS was fully charged during the 16th, 17th, and 18th hours, and excess solar energy into the SR3 was loss as spillage. Alternatively, spillage could have been alleviated by using a partial on-sun dispatch during the 10th hour. The system generated at the 111.7 MWe rated power for up to a total of 13.80 hours (7.80 on-sun and 6 off-sun) with a system energy efficiency of 26.76%.

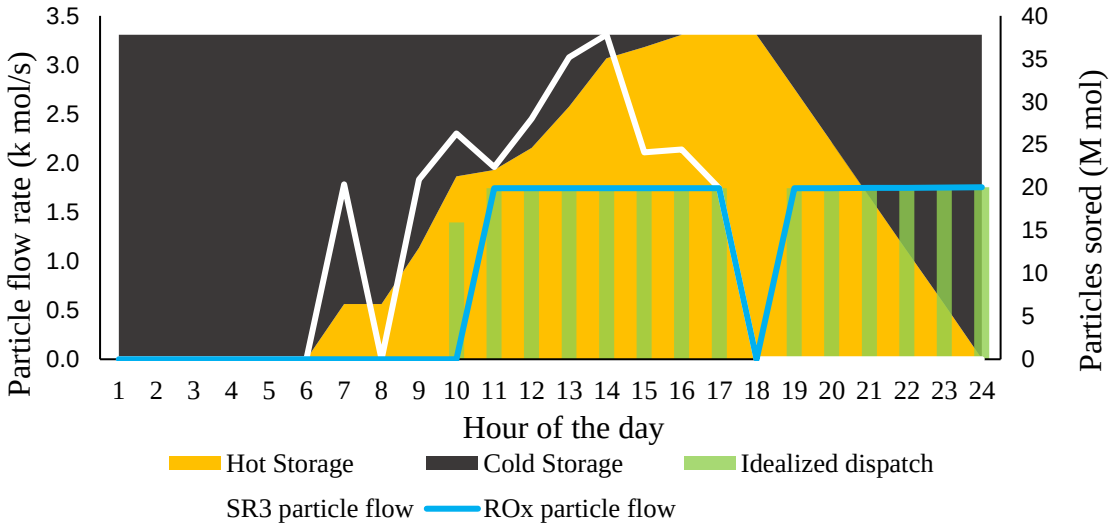

Figure 7. Dispatch schedule for spring equinox (April 17) using Barstow solar data

Figure 8 below shows the summer solstice case study (high solar). The particles began flowing through the SR3 during the 7th hour and stopped flowing during the 17th hour. The power block generated on-sun power between the 9th and 17th hours, and

generated off-sun power between the 19th and 24th hours. The HS was fully charged during the 15th, 16th, and 18th hours, which caused significant spillage losses in this high solar case and this dispatch schedule. The system generated at rated power for a total of 17.88 hours (11.88 on-sun and 6 off-sun) with a system energy efficiency of 26.36%.

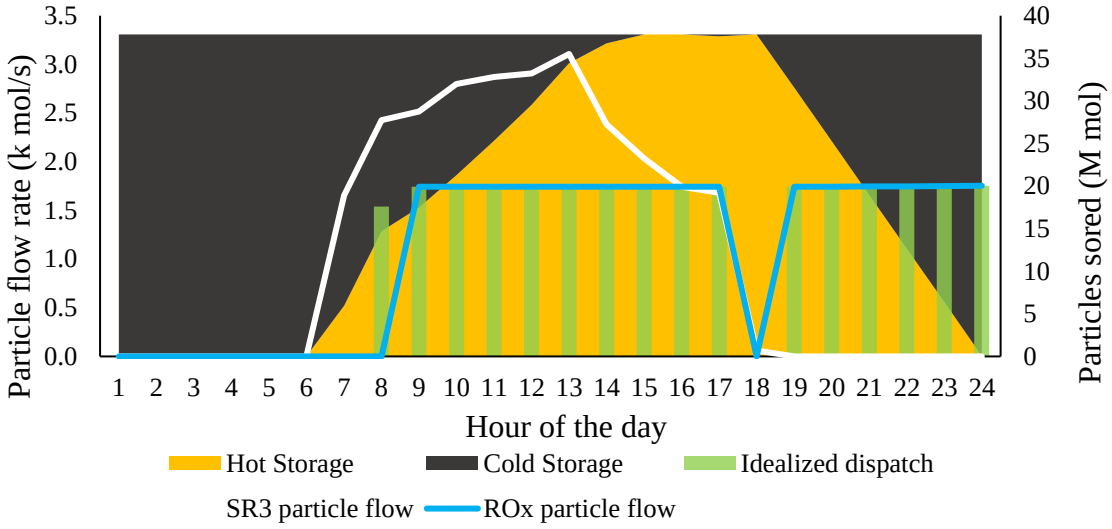

Figure 8. Dispatch schedule for summer solstice (June 14) using Barstow solar data

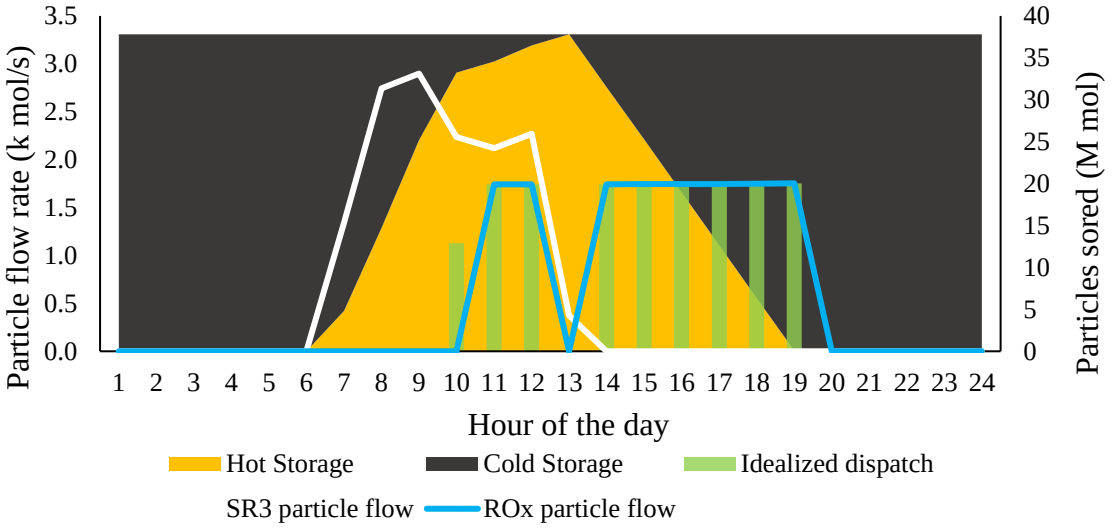

Figure 9. Dispatch schedule for winter solstice (March 12) using Barstow solar data

Figure 9 above shows the winter solstice case study (low solar). The particles flowed through the SR3 between the 7th and 13th hours. The power block generated on-sun power only during the 11th and 12th hours, and generated off-sun power between the 14th and 19th hours. The HS was fully charged in the 13th hour and experienced moderate spillage. Alternatively, spillage could have been alleviated by using a partial on-sun dispatch during the 10th hour. The system generated at rated power for up to a total of 8.65 hours (2.65 on-sun and 6 off-sun) with a system energy efficiency of 26.87%.

The intermediate values, which are functions of input values from Table 10, for Figs. 7, 8, and 9 are shown in Table 12. For instance, δ is a function of T_4 and $P_{O_2}^{SR3}$, A_{SM}^{sf} is a function of A_1^{sf} and SM, $r_{h,ins}^{SR3}$ is a function of γ_{cav} and other values, and V^{HS} is a function of N_p and other values. See the section 3.1 for the complete equation set for these intermediate values. Also shown in Table 12, however, are the results for the pseudo-annual performance metrics given the three case study days displayed in Figs. 7, 8, and 9. The current nominal system design achieved an annual system energy efficiency of 24.40% and capacity factor of 52.24%.

Table 12. Intermediate values and output performance metrics

Term	Value	Units
δ	0.205	-
A_{SM}^{sf}	778,338	m^2
$r_{h,ins}^{SR3}$	0.84	m
$r_{c,body}^{SR3}$	1.00	m
L^{SR3}	1.68	m
V^{HS}	2209.74	m^3
V^{CS}	2209.74	m^3
CF_{sys}	52.24	%
$\eta_{E,sys}$	24.40	%

Initial sensitivity analyses were performed on the functions for extent of reduction (δ) and particle energy density. The extent of reduction is a function of the maximum temperature (T_4) and the partial pressure of oxygen ($P_{O_2}^{SR3}$) inside the SR3. Figure 10 shows that δ increases approximately linearly with increasing temperature and increases logarithmically with decreasing partial pressure of oxygen. As expected for the endothermic chemical reaction with a gas phase product, higher temperatures and lower partial pressure increases reduction extent. Nominal values for the results section considers 1050 °C temperature and 200 Pa particle pressure oxygen inside the SR3, which corresponds to a δ of 0.205 for CAM28.

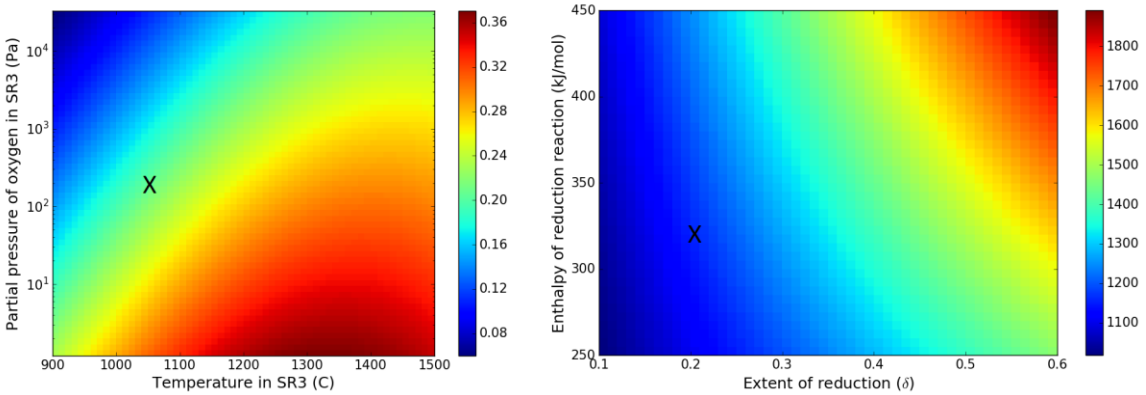

Figure 10. (left) Response map of δ as a function of SR3 partial pressure of oxygen and temperature.

Figure 11. (right) Response map of particle energy density as a function of δ and enthalpy of reduction if discharged between 1050 °C and 200 °C.
Nominal system values are indicated by "X".

Figure 11 shows that the energy density scales approximately linearly as a function of δ and the enthalpy of the reduction reaction (ΔH_{rxn}). Energy density may be increased by increasing the amount of sensible energy and the amount of chemical energy stored per unit mass particle. The two terms considered here only effect the amount of chemical energy stored, however. To increase chemical energy storage density, improved

materials may have higher enthalpy of reduction reaction or achieve higher extent of reduction, although they tend to work in opposite directions. Nominal values for the results section considers a δ of 0.205 and H_{rxn} of 320 kJ/mol-O_2, which results in an energy density of approximately 1170 kJ/kg.

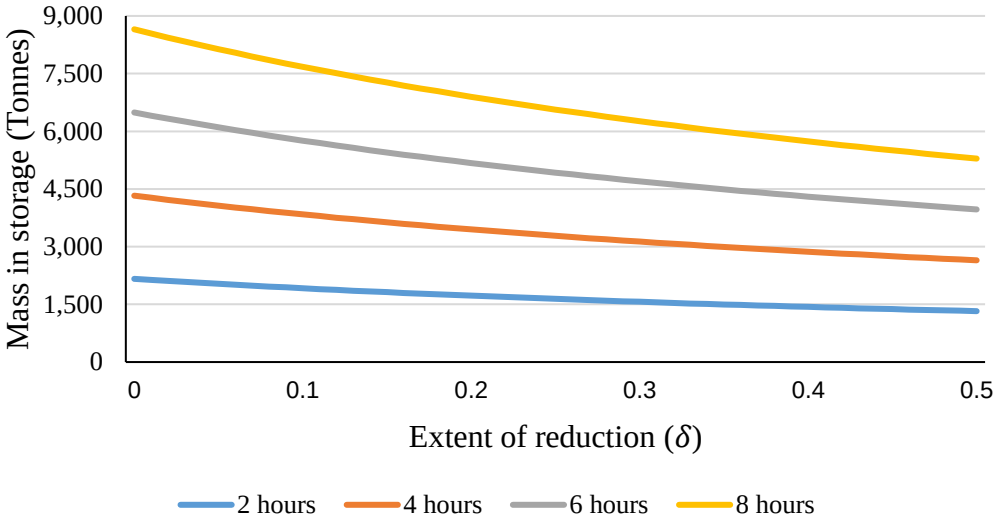

Figure 12. Sensitivity analysis of two to eight hours of storage and various extent of reduction on CAM28 mass in storage

System performance and design criteria for multiple off-sun storage hours and solar multipliers are shown in Figs. 12 and 13. Figure 12 displays the total mass of particles (in metric tons) residing in the 111.7 MWe system for δ ranging from 0 to 0.5 and off-sun generation targets from 2 hours to 8 hours. The amount of particles for 8 hours of storage goes from a high of about 8,630 Tonnes at $\delta = 0$ (sensible only) to a low of about 5,280 Tonnes at $\delta = 0.5$, which is a reduction of 38.9% in storage mass. The amount of particles for 2 hours of storage goes from a high of about 2,160 Tonnes at $\delta = 0$ to a low about 1,320 Tonnes at $\delta = 0.5$, which is also a reduction of 38.9% in

storage mass. Therefore, δ can substantially affect the amount of particles flowing through the system.

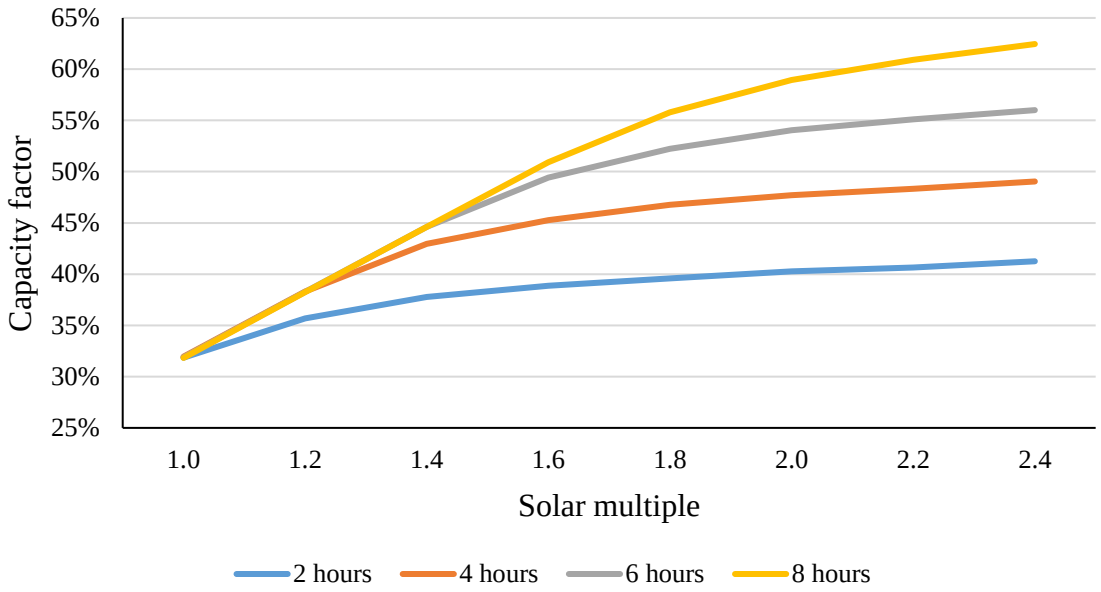

Figure 13. Sensitivity analysis of two to eight hours of storage and various solar multiples on capacity factor

Figure 13 shows results for pseudo-annual capacity factor under different storage capacities and solar multiples. The maximum capacity factor of a power generation plant is 100%, which corresponds to a power plant continuously generating electricity for 24 hours a day for 365 days of the year. Renewable energy, however, seldom reach such high capacity factors because of solar and wind resources are variable and would require excessive storage. Figure 13 shows that the capacity factor begins by linearly increasing directly with the solar multiple, but experiences diminishing returns due to spillage depending on the storage capacity included. The nominal system design, sized at 1.8 solar multiple with six hours of storage, achieves a capacity factor of 52.24%. Nominal system design can be improved in two ways: increase the installed storage capacity to 8 hours for

an increased capacity factor of 56.39%, or decrease the solar multiple to increase the ratio of capacity factor to solar multiple.

Annual system energy efficiency is evaluated with a sensitivity analysis on 9 system design parameters in Figs. 14 and 15. Figure 14 illustrates the effect of the solar multiple, δ, heat exchanger contact area (A^{HX}), and γ_{cav} on annual system energy efficiency. Of the four terms considered, changes to the solar multiple has the most significant on energy efficiency. A 30% decrease (increase) in solar multiple corresponds to approximately 0.7% increase (1.3% decrease) in energy efficiency. In contrast, there is a negligible effect from A^{HX} (less than 0.06% overall), suggesting that the SR3's oxygen heat recuperation will not significantly effect system performance.

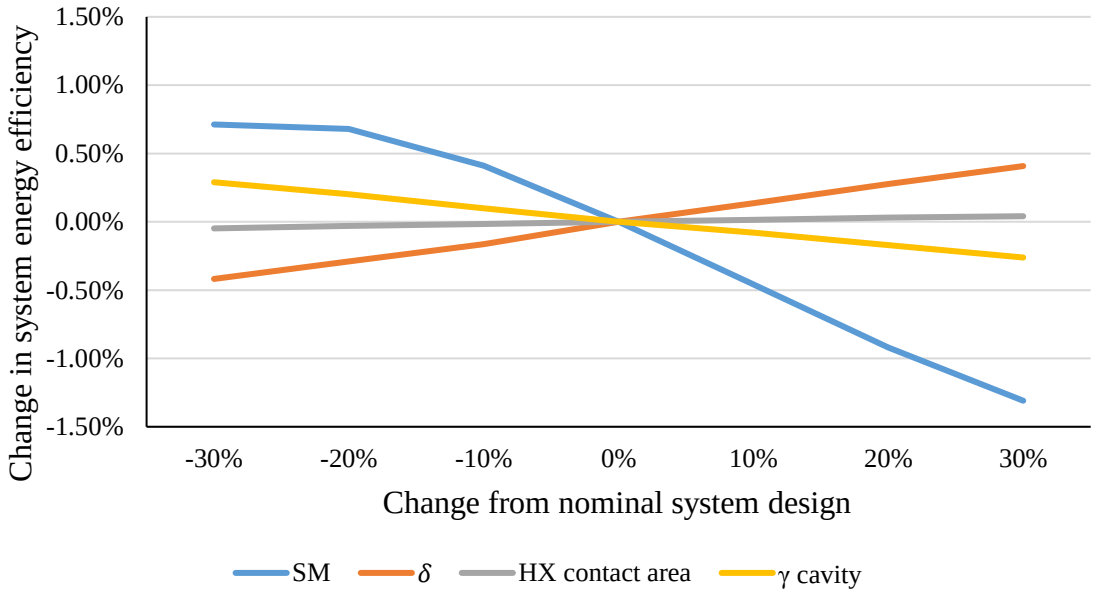

Figure 14. Sensitivity analysis of system design parameters on system energy efficiency

Figure 15 illustrates the effect of changing the thermal resistances of the ROx, SR3, HS, and CS components on system energy efficiency by performing a sensitivity analysis on the thickness of the insulating materials. The change in system energy

efficiency is evaluated using these thickness terms at 50%, 100%, and 150% of nominal system design. The color green (red) corresponds to a 50% increase (decrease) in thickness of the insulation material. The HS and CS case, however, is under an idealized dispatch schedule that dispatches immediately opposed to any after midnight dispatch or early morning dispatch. The HS operates at higher temperatures than the CS, and therefore should be more susceptible to increased and decreased thermal resistance (thermal conductivity and insulation thickness).

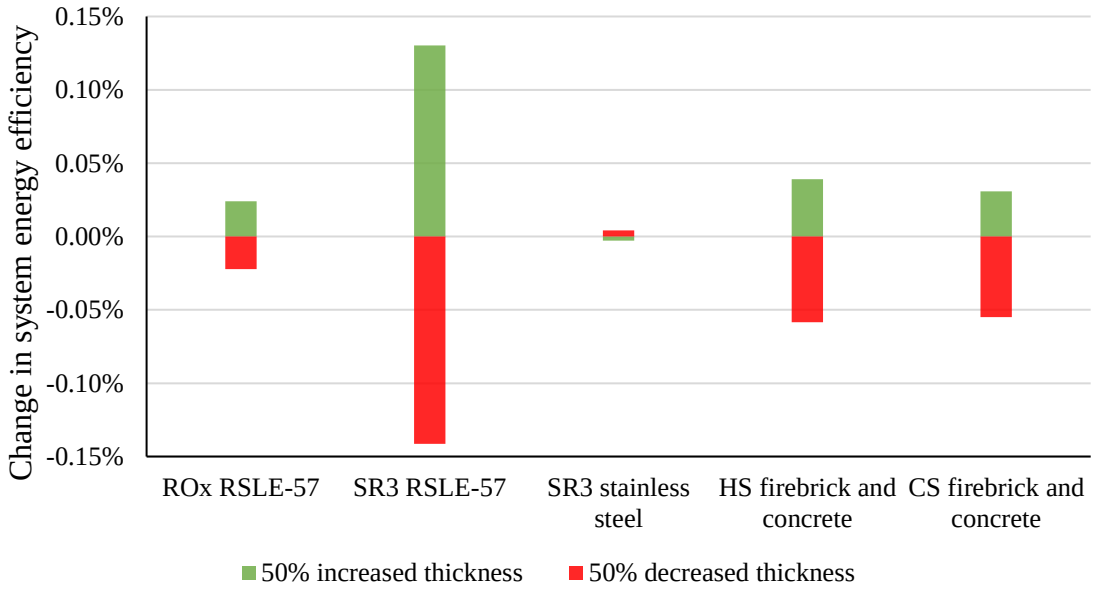

Figure 15. Sensitivity analysis of various insulation material thicknesses on system energy efficiency

Figure 15 shows that the SR3 stainless steel insulation layer is an anomaly, because increased thickness results in less system energy efficiency. The total heat loss term for the SR3 is a radial thermal circuit in series with four resistances that depend on each other. As the thickness of the SR3 layers increase, the outer SR3 surface area also increases; thus, an increased resistance (via thickness) in the stainless-steel layer results in decreased resistance of free convection on the exterior. Despite the inverse relationship

of the SR3 stainless steel insulation, the SR3 alumina insulation demonstrates the largest response of 0.13% increase and 0.14% decrease on system energy efficiency. The HS has a higher gain in efficiency (+0.04% vs +0.03%) and higher loss in efficiency (-0.06% vs -0.05%) than the CS as the insulation thickness is increased and decreased, respectively, because the HS must insulate higher temperature particles than the CS.

5. CONCLUSIONS

The work presented here uses a thermodynamic mass and energy balance component performance model to help design and assess the application and potential for commercialization of 111.7 MWe concentrating solar power (CSP) system coupled with solar thermochemical energy storage using redox active metal oxides. The novel CSP system includes five major components (ROx, SR3, HS, CS, HX), two small components (vacuum pump, particle lift), and two boundary components (solar field, air Brayton turbine with a bottoming steam cycle). The model was used to size components, simulate intraday dispatch performance, measure average annual energy efficiency and capacity factor, and perform sensitivity analysis of component and material parameters.

Results indicate that that the maximum marginal capacity factor was around 32%—i.e., maximum increase in capacity factor per solar multiple. At nominal system configuration, with storage size of six hours and solar multiple of 1.8, the capacity factor was 52.73% which is less than 56.39% achieved by sizing the storage for eight hours of off-sun generation. Therefore, the net capacity factor can be increased. To further improve the capacity factor per solar multiple, either storage size should be increased or solar multiple should be decreased.

The change in annual system energy efficiency was evaluated by performing a sensitivity analysis on the design parameters of nine system and component parameters. Higher solar multiples consistently decreased efficiency, because large plants require larger components that become more difficult to scale. Conversely, higher extent of reduction increased efficiency, because a larger fraction of energy is held and maintained in a chemical reaction instead of sensible heat. As expected, the heat exchanger that

recuperates energy from high temperature oxygen provided negligible increase of less than 0.06% in system energy efficiency as size of the contact area was increased and decreased by 30%. The component that benefited the most from additional insulation material is the SR3. Extra RSLE-57 insulation in the SR3 was shown to provide up to 0.13% extra system-wide energy efficiency if the thickness of RSLE-57 was increased by 50%. The SR3 stainless steel insulation, however, should be minimized, while remaining structurally sound because it had a negative effect on system energy efficiency.

Future thermodynamic work can investigate higher detailed models for the solar field, the SR3, ROx, and air Brayton components. The solar field boundary model uses a nominal efficiency term without considering blocking and shading, time of day and year, latitude, wind outages, heliostat design, and reflectivity. Additional air Brayton turbine models and operating states can be explored other than the Ansaldo Energia AE64.3A model considered here. For instance, a turbine with a lower or higher air compression ratio, with different air mass flow rates, or with a recuperator. Higher fidelity thermodynamic models for components can be integrated—e.g., complex fluid dynamics for ROx reactor. Improved time series modeling that simulate system operation using higher time scale resolutions can create finer dispatch schedule—e.g., minutes instead of hours—and productivity results or a full year rather than three representative days. These higher fidelity models can also explore the warm-up and cool-down transient plant operations. Forthcoming work will couple economic parameters with this thermodynamic model to perform an in depth technoeconomic analysis.

REFERENCES

[1] REN21. (2016). *Renewables 2016 Global Status Report.* Paris; France: Ren21 Secretariat. Retrieved from http://www.ren21.net/wp-content/uploads/2016/10/REN21_GSR2016_FullReport_en_11.pdf

[2] U.S. Energy Information Administration. (2016). *Annual Energy Outlook 2016 with projections to 2040.* Washington DC: U.S. Retrieved from https://www.eia.gov/outlooks/aeo/pdf/0383(2016).pdf

[3] Fu, R., Chung, D., Lowder, T., Feldman, D., Ardani, K., & Margolis, R. (2016). U.S. Solar Photovoltaic System Cost Benchmark: Q1 2016. doi:10.2172/1326888

[4] International Energy Agency PVPS. (2016). *Trends 2016 in Photovoltaic Applications.* Retrieved rom http://www.iea-pvps.org/fileadmin/dam/public/report/national/Trends_2016_-_mr.pdf

[5] GlobalData. (June 27, 2016). Global Installed Solar Photovoltaic Capacity Will Exceed 756 GW by 2025, says GlobalData. Retrieved from http://energy.globaldata.com/media-center/press-releases/power-and-resources/global-installed-solar-photovoltaic-capacity-will-exceed-756-gw-by-2025-says-globaldata

[6] Mendelsohn, M., Lowder, T., & Canavan, B. (2012). Utility-Scale Concentrating Solar Power and Photovoltaic Projects: A Technology and Market Overview. doi:10.2172/1039803

[7] U.S. Department of Energy. (2014). [Map depicting concentrating solar power plants across the U.S.] *MAP: Concentrating Solar Power Across the United States.* Retrieved from https://energy.gov/articles/map-concentrating-solar-power-across-united-states

[8] Behar, O., Khellaf, A., & Mohammedi, K. (2013). A review of studies on central receiver solar thermal power plants. Renewable and Sustainable Energy Reviews, 23, 12–39. doi:10.1016/j.rser.2013.02.017

[9] Stoddard, L., Abiecunas, J., & O'Connell, R. (2006). Economic, Energy, and Environmental Benefits of Concentrating Solar Power in California. doi:10.2172/881924

[10] Price, H., & Kearney, D. (2003). Reducing the Cost of Energy From Parabolic Trough Solar Power Plants. Solar Energy. doi:10.1115/isec2003-44069

[11] Gil, A., Medrano, M., Martorell, I., Lázaro, A., Dolado, P., Zalba, B., & Cabeza, L. F. (2010). State of the art on high temperature thermal energy storage for power generation. Part 1—Concepts, materials and modellization. Renewable and Sustainable Energy Reviews, 14(1), 31–55. doi:10.1016/j.rser.2009.07.035

[12] Denholm, P., & Hummon, M. (2012). Simulating the Value of Concentrating Solar Power with Thermal Energy Storage in a Production Cost Model. doi:10.2172/1059140

[13] Denholm, P., O'Connell, M., Brinkman, G., & Jorgenson, J. (2015). Overgeneration from Solar Energy in California. A Field Guide to the Duck Chart. doi:10.2172/1226167

[14] REN21. (2015). *Renewables 2015 Global Status Report.* Paris; France: Ren21 Secretariat. Retrieved from http://www.ren21.net/wp-content/uploads/2015/07/REN12-GSR2015_Onlinebook_low1.pdf

[15] U.S. Department of Energy. (2012). SunShot Vision Study: February 2012 (Book). doi:10.2172/1039075

[16] U.S. Department of Energy. (n.d.) Project Profile: High Performance Reduction/Oxidation Metal Oxides for Thermochemical Energy Storage. Retrieved from http://energy.gov/eere/sunshot/project-profile-high-performance-reductionoxidation-metal-oxides-thermochemical-energy

[17] Glatzmaier, G. (2011). Summary Report for Concentrating Solar Power Thermal Storage Workshop: New Concepts and Materials for Thermal Energy Storage and Heat-Transfer Fluids, May 20, 2011. doi:10.2172/1022291

[18] Vignarooban, K., Xu, X., Arvay, A., Hsu, K., & Kannan, A. M. (2015). Heat transfer fluids for concentrating solar power systems–a review. Applied Energy, 146, 383-396.

[19] Tian, Y., & Zhao, C. Y. (2013). A review of solar collectors and thermal energy storage in solar thermal applications. Applied Energy, 104, 538-553.

[20] National Renewable Energy Laboratory. (n.d.). Concentrating Solar Projects [CSV data file]. Retrieved from https://www.nrel.gov/csp/solarpaces/

[21] Zalba, B., Marín, J. M., Cabeza, L. F., & Mehling, H. (2003). Review on thermal energy storage with phase change: materials, heat transfer analysis and applications. Applied Thermal Engineering, 23(3), 251–283. doi:10.1016/s1359-4311(02)00192-8

[22] Farid, M. M., Khudhair, A. M., Razack, S. A. K., & Al-Hallaj, S. (2004). A review on phase change energy storage: materials and applications. Energy Conversion and Management, 45(9-10), 1597–1615. doi:10.1016/j.enconman.2003.09.015

[23] Kuravi, S., Trahan, J., Goswami, D. Y., Rahman, M. M., & Stefanakos, E. K. (2013). Thermal energy storage technologies and systems for concentrating solar power plants. Progress in Energy and Combustion Science, 39(4), 285–319. doi:10.1016/j.pecs.2013.02.001

[24] Shabgard, H., Faghri, A., Bergman, T. L., & Andraka, C. E. (2013). Numerical Simulation of Heat Pipe-Assisted Latent Heat Thermal Energy Storage Unit for Dish-Stirling Systems. Journal of Solar Energy Engineering, 136(2), 021025. doi:10.1115/1.4025973

[25] Sharifi, N., Faghri, A., Bergman, T. L., & Andraka, C. E. (2015). Simulation of heat pipe-assisted latent heat thermal energy storage with simultaneous charging and discharging. International Journal of Heat and Mass Transfer, 80, 170–179. doi:10.1016/j.ijheatmasstransfer.2014.09.013

[26] Gil, A., Medrano, M., Martorell, I., Lázaro, A., Dolado, P., Zalba, B., & Cabeza, L. F. (2010). State of the art on high temperature thermal energy storage for power generation. Part 1—Concepts, materials and modellization. Renewable and Sustainable Energy Reviews, 14(1), 31–55. doi:10.1016/j.rser.2009.07.035

[27] Pardo, P., Deydier, A., Anxionnaz-Minvielle, Z., Rougé, S., Cabassud, M., & Cognet, P. (2014). A review on high temperature thermochemical heat energy storage. Renewable and Sustainable Energy Reviews, 32, 591–610. doi:10.1016/j.rser.2013.12.014

[28] Project Staff. (2011). Thermochemical heat storage for concentrated solar power. doi:10.2172/1039304

[29] Neises, M., Tescari, S., de Oliveira, L., Roeb, M., Sattler, C., & Wong, B. (2012). Solar-heated rotary kiln for thermochemical energy storage. Solar Energy, 86(10), 3040–3048. doi:10.1016/j.solener.2012.07.012

[30] Ho, C. K., & Iverson, B. D. (2014). Review of high-temperature central receiver designs for concentrating solar power. Renewable and Sustainable Energy Reviews, 29, 835–846. doi:10.1016/j.rser.2013.08.099

[31] Babiniec, S. M., Coker, E. N., Miller, J. E., & Ambrosini, A. (2015). Investigation of LaxSr1−xCoyM1−yO3−δ (M=Mn, Fe) perovskite materials as thermochemical energy storage media. Solar Energy, 118, 451–459. doi:10.1016/j.solener.2015.05.040

[32] Babiniec, S. M., Coker, E. N., Miller, J. E., & Ambrosini, A. (2015). Doped calcium manganites for advanced high-temperature thermochemical energy storage. International Journal of Energy Research, 40(2), 280–284. doi:10.1002/er.3467

[33] Ho, C. K. (2008). Software and codes for analysis of concentrating solar power technologies. doi:10.2172/946571

[34] Blair, N., Dobos, A. P., Freeman, J., Neises, T., Wagner, M., Ferguson, T., … Janzou, S. (2014). System Advisor Model, SAM 2014.1.14: General Description. doi:10.2172/1126294

[35] Yao, Z., Wang, Z., Lu, Z., & Wei, X. (2009). Modeling and simulation of the pioneer 1MW solar thermal central receiver system in China. Renewable Energy, 34(11), 2437–2446. doi:10.1016/j.renene.2009.02.022

[36] Wei, X., Lu, Z., Wang, Z., Yu, W., Zhang, H., & Yao, Z. (2010). A new method for the design of the heliostat field layout for solar tower power plant. Renewable Energy, 35(9), 1970–1975. doi:10.1016/j.renene.2010.01.026

[37] Llorente García, I., Álvarez, J. L., & Blanco, D. (2011). Performance model for parabolic trough solar thermal power plants with thermal storage: Comparison to operating plant data. Solar Energy, 85(10), 2443–2460. doi:10.1016/j.solener.2011.07.002

[38] Nithyanandam, K., & Pitchumani, R. (2011). Analysis and optimization of a latent thermal energy storage system with embedded heat pipes. International Journal of Heat and Mass Transfer, 54(21-22), 4596–4610. doi:10.1016/j.ijheatmasstransfer.2011.06.018

[39] Nithyanandam, K., Pitchumani, R., & Mathur, A. (2014). Analysis of a latent thermocline storage system with encapsulated phase change materials for concentrating solar power. Applied Energy, 113, 1446–1460. doi:10.1016/j.apenergy.2013.08.053

[40] Nithyanandam, K., & Pitchumani, R. (2014). Cost and performance analysis of concentrating solar power systems with integrated latent thermal energy storage. Energy, 64, 793–810. doi:10.1016/j.energy.2013.10.095

[41] Stekli, J., Irwin, L., & Pitchumani, R. (2013). Technical Challenges and Opportunities for Concentrating Solar Power With Thermal Energy Storage. Journal of Thermal Science and Engineering Applications, 5(2), 021011. doi:10.1115/1.4024143

[42] Bell, I. H., Wronski, J., Quoilin, S., & Lemort, V. (2014). Pure and Pseudo-pure Fluid Thermophysical Property Evaluation and the Open-Source Thermophysical Property Library CoolProp. Industrial & Engineering Chemistry Research, 53(6), 2498–2508. doi:10.1021/ie4033999

[43] Ermanoski, I., Siegel, N. P., & Stechel, E. B. (2013). A New Reactor Concept for Efficient Solar-Thermochemical Fuel Production. Journal of Solar Energy Engineering, 135(3), 031002. doi:10.1115/1.4023356

[44] Zhang, Y., Smith, S. J., Kyle, G. P., & Stackhouse, P. W. (2010). Modeling the potential for thermal concentrating solar power technologies. Energy Policy, 38(12), 7884–7897. doi:10.1016/j.enpol.2010.09.008

[45] The Engineering Toolbox. (n.d.). *Drag Coefficient* [Online data table]. Retrieved from http://www.engineeringtoolbox.com/drag-coefficient-d_627.html

[46] Jaeger, H. M., & Nagel, S. R. (1992). Physics of the Granular State. Science, 255(5051), 1523–1531. doi:10.1126/science.255.5051.1523

[47] Ansaldo Energia. (2013). *AE64.3A Gas Turbine.* Retrieved from http://ansaldoenergia.it/easyUp/file/gas_turbine_ae64_3a_june2013.pdf

[48] Imponenti, L., Albrecht, K. J., Braun, R. J., & Jackson, G. S. (2016). Measuring Thermochemical Energy Storage Capacity with Redox Cycles of Doped-CaMnO3. ECS Transactions, 72(7), 11–22. doi:10.1149/07207.0011ecst

[49] Ehrhart, B., & Gill, D. (2013). Evaluation of annual efficiencies of high temperature central receiver concentrated solar power plants with thermal energy storage. doi:10.2172/1090218

[50] Eddhibi, F., Amara, M. B., Balghouthi, M., & Guizani, A. (2015). Optical study of solar tower power plants. Journal of Physics: Conference Series, 596, 012018. doi:10.1088/1742-6596/596/1/012018

[51] Schrader, A. J., Muroyama, A. P., & Loutzenhiser, P. G. (2015). Solar electricity via an Air Brayton cycle with an integrated two-step thermochemical cycle for heat storage based on Co3O4/CoO redox reactions: Thermodynamic analysis. Solar Energy, 118, 485–495. doi:10.1016/j.solener.2015.05.045

[52] Mikron Instrument Company, Inc. (n.d.). *Table of emissivity of various surfaces.* Retrieved from http://www-eng.lbl.gov/~dw/projects/DW4229_LHC_detector_analysis/calculations/emissivity2.pdf

[53] ZIRCAR Refractory Composites, Inc. (2005). *Silica composite materials* [Data sheet]. Retrieved from http://www.zrci.com/wdpr/wp-content/uploads/2016/05/zrci201.pdf\

[54] Aerospace Specification Metals, Inc. (n.d.). *AISI Type 304 Stainless Steel.* Retrieved from http://asm.matweb.com/search/SpecificMaterial.asp?bassnum=MQ304A

[55] Christy Refractories. (2004). *Insulating firebrick* [Data sheet]. Retrieved from http://www.christyco.com/pdf/crc/Insulating_Firebrick_Data_Sheet.pdf

[56] Perlite Institute, Inc. (2014). *Overview of perlite concrete* [Data sheet]. Retrieved from https://www.perlite.org/library-perlite-info/construction-perlite/Perlite-Concrete.pdf

[57] Kanbur, B. B., Atayilmaz, S. O., Demir, H. A. K. A. N., Koca, A. L. I. I. H. S. A. N., & Gemici, Z. A. F. E. R. (2013). Investigating the thermal conductivity of different concrete and reinforced concrete models with numerical and experimental methods. Recent Advances in Mechanical Engineering Applications, Recent Advances in Mechanical Engineering Series, (8), 95-101.

[58] The Engineering Toolbox. (n.d.). *Heat Exchanger Heat Transfer Coefficients* [Online data table]. Retrieved from http://www.engineeringtoolbox.com/heat-transfer-coefficients-exchangers-d_450.html

[59] de la Vergne J. (2003). Hard Rock Miner’s Handbook, 3rd Ed. McIntosh Engineering Limited. Tempe, AZ, 215.

[60] National Renewable Energy Laboratory. (n.d.). *National Solar Radiation Data Base* [CSV data file]. Retrieved from http://rredc.nrel.gov/solar/old_data/nsrdb/1991-2005/tmy3/by_state_and_city.html